DEVELOPMENT AND INTEGRATION OF WAVEFRONT SHAPING TECHNIQUES IN A MULTIPARAMETRIC MICROSCOPE

by

DIVARIS GERASIMOS

Submitted in partial fulfillment of the requirements for the degree of
MSc in Photonics and Nanoelectronics

Department of Physics

UNIVERSITY OF CRETE

[19 June, 2023]

UNIVERSITY OF CRETE

DEPARTMENT OF PHYSICS

We hereby approve the thesis of

DIVARIS GERASIMOS

candidate for the degree of **MSc in Photonics and Nanoelectronics**

Committee Chair

Prof. Makris Konstantinos

Committee Member

Dr. Zacharakis Giannis

Committee Member

Prof. Kominis Iannis

Date of Defense

19 June 2023

DEDICATION

To my loving family and friends,

I dedicate this thesis to you, with unfeigned appreciation for the sacrifices and support you have given me throughout my academic journey.

Sincerely,

Gerasimos

TABLE OF CONTENTS

LIST OF FIGURES

ACKNOWLEDGEMENTS

I would like to utilize this opportunity to express my heartfelt gratitude to the many people that have helped me, guided me, and supported me in this academic journey. First and foremost, I would like to thank my supervisor, Dr. Zacharakis for giving me the chance to be a part of one of the best research groups in the field of Biophotonics and Bioimaging. Moreover, I want to sincerely thank Mr. Mavrakis for tirelessly guiding me from the very first moment I set foot in the laboratory. His deep scientific knowledge and his patience have shown me the way to become a better scientist and have prepared me appropriately to overcome any upcoming obstacles. His mentorship has made a lasting impact on my life and career, and I will always be grateful for his support. Lastly, I would like to thank Mr. Mylonakis, Mr. Marakis, and the rest of the members of the research group for providing an extra layer of help and guidance throughout this year.

DEVELOPMENT AND INTEGRATION OF WAVEFRONT SHAPING TECHNIQUES IN A MULTIPARAMETRIC MICROSCOPE

Abstract

by

DIVARIS GERASIMOS

Developing already existing microscopy systems by introducing new techniques and means or creating new microscopes is a vital part to better studying biological samples or systems and making advances in medical-related fields. By combining many different methods in a multiparametric microscope, such as two-photon microscopy, Raman spectroscopy, and photoacoustic imaging and further enhancing the standalone techniques can result in the imaging of different types of biological molecules at the same time. In addition to the reduction in imaging time achieved through the concurrent utilization of multiple techniques, the complementary nature of these methods allows for the acquisition of supplementary information, resulting in more comprehensive and detailed final images and in better understanding of the sample itself. Therefore, this represents a leap forward towards more accurate surgical procedures and more targeted medical treatments. In this Master thesis, the main goal was to improve photoacoustic imaging by introducing a Bessel Beam in the place of the Gaussian one and manipulating the Bessel beam with wavefront shaping techniques in order to suppress its side lobes and retain mainly the central lobe with the maximum intensity (Droplet Beam). By achieving this, due to the non-diffracting properties of the Bessel beam, we would attain a much larger imaging depth than with its Gaussian counterpart because of the greater Depth Of Field of this beam and therefore be able to get photoacoustic images in much greater depths in biological

tissue than ever before along with higher resolution. The use of this greater imaging depth is dictated by the nature of the biological samples that have curvature and consist of many layers. With the use of a Gaussian beam, we can image a single layer in high resolution while with the utilization of this so-called Droplet beam, we would be able to image multiple layers at high resolution simultaneously.

Chapter 1

INTRODUCTION

Eyes are the window to the soul. This is a common poetic saying that has been proven to be true to some degree. Recent studies in the field of Biology suggest that one's eyes may not be a window to the soul but may be a window to one's brain. Since the retina is considered to be a part of the Central Nervous System (CNS), a variety of neurogenerative conditions that mainly affect the brain may show early indicators in the ocular cavity. In fact, the retina is the only part of the CNS to be exposed to the outside and therefore the most accessible part of the CNS to us. Thus, by effectively examining the eyes we may be able to predict and even halt the development of diseases such as Alzheimer's, Parkinson's, and Multiple Sclerosis Disease by treating them in the early stages [1].

These reasons have pushed us towards developing a new multiparametric microscope that combines multiple methods such as two-photon excitation, Raman spectroscopy, and photoacoustic imaging and may be the leap forward towards detecting infinitesimal deteriorations in the retina. Furthermore, our intuition was to manipulate the Gaussian beam that is typically used in photoacoustic imaging and turn it into a Bessel Beam with suppressed side lobes. Because the central maximum of a Bessel Beam seems to retain its form and intensity profile for much greater propagation distances than its Gaussian counterpart it is considered to be a better and more promising alternative. Due to this property, we should be able to achieve deeper and better-quality soft tissue imaging, since the depth of field of the beam is significantly greater[2].

However, even though the generation of a Bessel Beam may be trivial, the suppression of the side lobes demands extremely precise wavefront shaping techniques to effectively cancel them and retain this cancelation for a minimum necessary

distance. Two methods were used to achieve this. The first one was to interfere two Bessel beams that follow two different optical paths and their interference be constructive in the central maximum and destructive in the remaining concentric maxima. The other way was to use a Spatial Light Modulator (SLM) and by micro manipulating the phase of each separate wavefront to produce a nearly perfect side lobe-free Bessel Beam.

Additionally, when all these microscopy techniques are combined, a new issue arises. By combining two distinct imaging techniques such as two-photon microscopy which utilizes a near-infrared laser beam and photoacoustic imaging which utilizes a visible laser beam, the alignment process becomes exceedingly challenging. This integration gives rise to significant optomechanical restrictions, particularly in terms of the optical elements employed. Lastly, the ultimate aim of the construction of this microscope is to be used in eye sample imaging, which sets us a limit to the amount of energy enclosed in the beam. If the energy is too high our biological samples may be destroyed entirely or partially, while if the energy is low enough, we may not be getting detailed images with high contrast. Therefore, for this microscope to be able to be used finally for in vivo bioimaging we need to strike a balance between the maximum and the minimum beam intensity.

Chapter 2

THEORETICAL BACKGROUND

2.1 Light Scattering

Light scattering is a phenomenon that occurs when light interacts with particles or structural features in a medium, causing the photons to deviate from their initial trajectory and disperse in the medium. More precisely, photons are more susceptible to strong scattering when their wavelength matches the dimensions of the structure that scatters them and the refractive index of the structure is different than that of the surrounding medium. In general, every light-scattering event can be described by the Mie scattering theory, which collapses to the special Rayleigh case if the wavelength is much greater than the dimensions of the scattering particles [3].

In any scattering medium, scatterers are randomly distributed in space, and thus photons can undergo many scattering events when passing through this medium. If the scatterer size and photon wavelength are much smaller than the mean distance between the particles in a medium then we can consider the medium to be loosely packed, if not, then it can be considered densely packed [3].

The characteristic length scale over which a particle can propagate before experiencing a collision is called the scattering mean free path. More exactly, the mean free path is the average distance a photon can travel between two scattering events and is denoted by the symbol l_s with units of length[3].

If we assume a single spherical scatterer with a cross-sectional area of σ_g and its scattering capability Q_s then the scattering coefficient of a medium with N_s scatterers can be given by the next equation[3]:

$$\mu_s = N_s \sigma_g Q_s, \tag{2.1}$$

where μ_s is the scattering coefficient and its reciprocal value is the scattering mean free path (l_s). If we want to quantify the probability of no scattering we can use Beer's law and then the ballistic transmittance will be[3]:

$$T(x) = exp(-\mu_s x), \tag{2.2}$$

If we analyze the absorption in a medium the same way as we did for the scattering we will get the following results. If we assume a single absorber in the medium with σ_g its cross-sectional area and Q_a the absorption efficiency then the absorption coefficient of the medium with N_a absorbers will be[3]:

$$\mu_a = N_a \sigma_g Q_a \tag{2.3}$$

As in the case of scattering, the mean absorption length (l_a will be the reciprocal value of μ_a. Combining the two coefficient values for absorption and scattering we can get the total interaction coefficient[3]:

$$\mu_t = \mu_a + \mu_s \tag{2.4}$$

The reciprocal value of the total interaction coefficient is the mean free path of the medium (Average length a photon will travel between two interaction events)[3]:

$$l_t = 1/\mu_t \tag{2.5}$$

We can introduce one more characteristic quantity for a medium and that is the transport mean free path. This variable refers to the average distance a photon will travel in its original trajectory after an infinite number of scattering events (l*).

2.2 Means of wavefront shaping

An inherent property of biological samples is that they scatter and absorb light and therefore cause distortions in the wavefront as it passes through them. This

distortion, necessarily, leads to degraded image quality, poor signal-to-noise ratio, and reduced resolution in bioimaging. For these distortions to be minimized, we can use a variety of techniques to manipulate the incident light's wavefront, before it enters the sample, in such a way that will become robust to scattering to an extent. This approach enhances image resolution and quality and it boosts the contrast of the acquired image too. Additionally, wavefront shaping techniques can, also, be exploited to selectively excite specific regions of the biological sample, such as individual cells or cellular structures. Essentially, wavefront shaping devices are connected to a sensor that detects and records the shape of the wavefront and then transmits this information to a computer. The shape of the wavefront is recorded after having passed through the biological sample too. The computer then analyzes the distortion caused by the biological sample and adjusts the wavefront shaping device to cancel out most of these distortions and aberrations. This leads to a real-time compensation of the signal loss in the most optimal way [4].

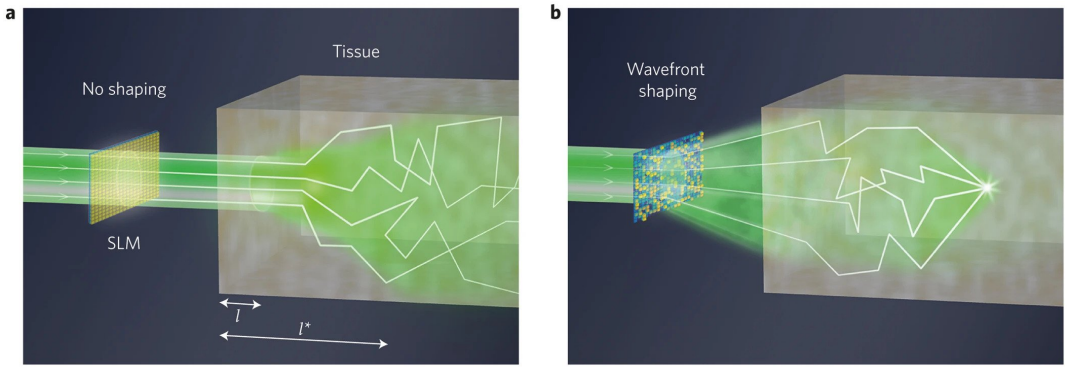

Figure 2.1: a) A coherent beam of light travels one mean free path (l) with minimal scattering into tissue. A portion of the beam's directionality remains conserved up to the transport mean free path length, l*. b) Wavefront-shaping of the incident beam, to focus within tissue beyond l* [4]

.

Several wavefront shaping elements used in bioimaging include:

- Deformable Mirrors (DMs)
- Digital Micromirror Devices (DMDs)

- Spatial Light Modulators (SLMs)
- Lenses
- Apertures

2.2.1 Deformable Mirrors

Deformable mirrors are optical objects with a reflective surface that can be deformed or moved by an array of actuators according to the will of the user to correct optical aberrations or manipulate and control the wavefront of the light. There are two types of Deformable mirrors. The first one is Continuous surface deformable mirrors and the second one is the segmented mirror. The quality of the deformable mirrors is determined primarily by the number of actuators they have because this number determines the degrees of freedom the mirror can correct. This number ranges from a few dozen to thousands. Usually, DMs are used to correct small optical aberrations and micromanage the wavefront [5].

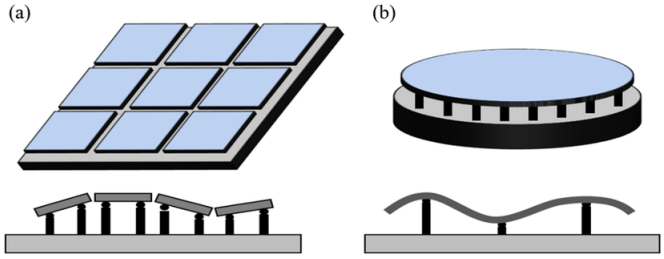

Figure 2.2: (a) Segmented and (b) continuous faceplate DM [6]

.

2.2.2 Digital Micromirror Devices

Digital Micromirror Devices (DMDs) are micro-electromechanical systems (MEMS) that are used to create patterns with light. DMDs consist of an array of tiny mirrors that can be individually tilted to reflect light in a certain direction. Each mirror is only a few micrometers in size and can be precisely controlled using an electronic

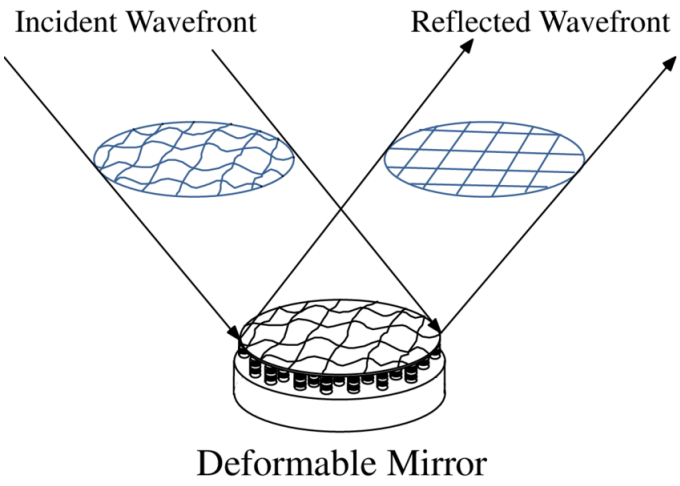

Figure 2.3: Wavefront phase conjugation using a deformable mirror [7]

.

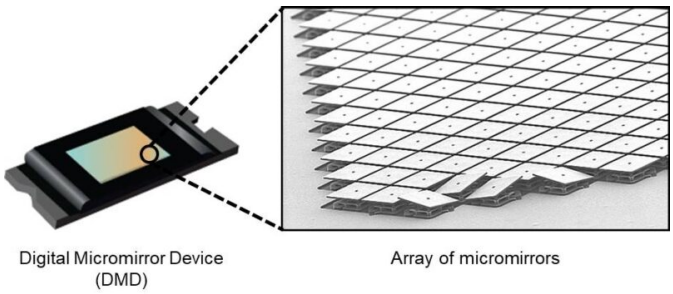

Figure 2.4: DMD and close up of an array of micro-mirrors in a DMD [8]

signal and corresponds to one pixel of the produced image. These micromirrors can only be switched between two distinct states that correspond to an "on" and "off". To produce the desired image each mirror is rapidly turned on and off with the help of a small applied voltage. The "off" state corresponds to a dark pixel and the "on" to a bright one. By controlling the speed of the switching between the two states and therefore the ratio of the "on" to "off" state, we can produce a greyscale value pixel (pulse width modulation). Modern DMDs can produce up to 1024 different greyscale value pixels. DMDs are considered optimal wavefront shaping devices when taking into consideration their refresh rate, as they can reach refresh rates up to 32kHz. On the contrary, as they are two-state devices, the amplitude modulation

they are capable of is only binary [8].

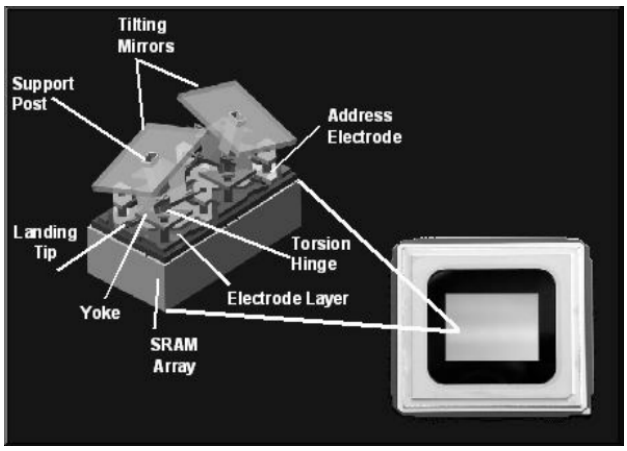

Figure 2.5: Schematic of two DMD mirror-pixels next to a typical DMD containing 1024*768 mirrors[8]

2.2.3 Spatial Light Modulators

A spatial light modulator is a device that can control the phase, the intensity of light, or both of them simultaneously. It usually consists of a great number of small pixels each of which can be controlled independently. There are two types of SLM systems, one is based on transmission and the other on reflection. Each pixel is constructed of a Liquid Crystal material. The electrical and optical anisotropy of LCs is the crucial reason they are being used in SLMs. Each greyscale value in the SLM device corresponds to a particular average voltage applied along the LC. Due to the aforementioned electrical anisotropy, LC molecules respond differently as they tilt differently with varying applied voltage. As mentioned before, LC molecules are optically anisotropic too. This means that due to the tilt, they acquire by the applied voltage, their refractive index is modified accordingly and this consequently results in a changed optical path within the LC cell. This difference in the optical path results in a gained phase difference. Therefore, when the SLM screen is reached by an incident beam with suitable polarization, it can provide different phase shifts for each pixel it has [9].

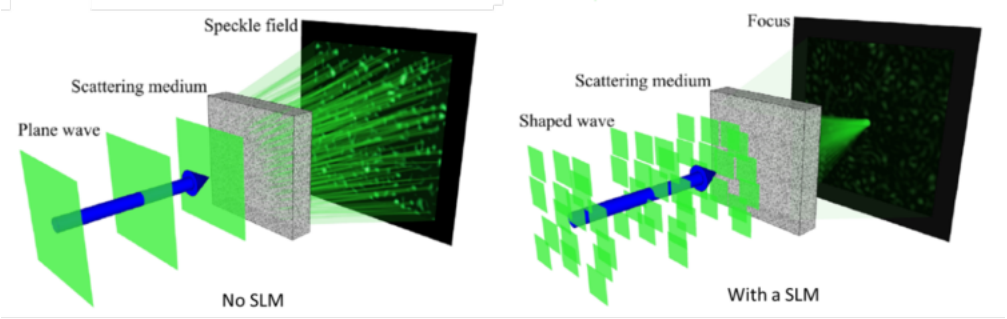

Figure 2.6: Hybridized wavefront shaping for high-speed, high-efficiency focusing through dynamic diffusive media [10]

Figure 2.7: Holoeye Pluto-2.1 Spatial Light Modulator [11]

2.2.4 Lenses

Even though this category may seem a trivial case of wavefront shaping, it is therefore still one of the most important means of wavefront shaping. There are two possible cases of "wavefront shaping" with the use of lenses. What ordinary spherical lenses do is that they Fourier transform the wavefront at a distance f from them and produce a Fourier pattern at a distance f after the lens. Thus essentially shaping the wavefront of the beam in unique ways. The other case we can have wavefront shaping with lenses is the case of special conical lenses such as axicons which can produce a superposition of plane waves lying their k-vectors on a cone and thus producing peculiar types of beams such as Bessel Beams [12].

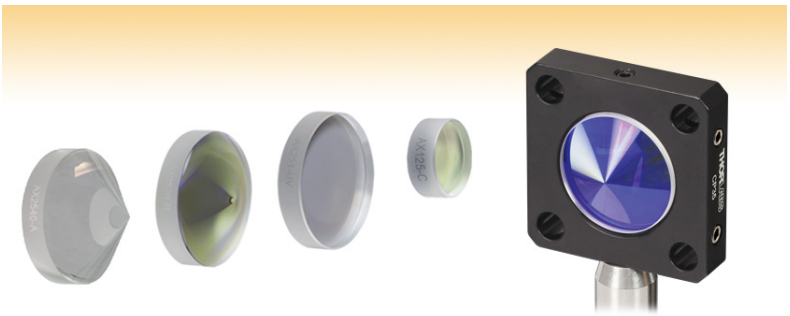

Figure 2.8: Thorlabs Fused Silica Axicons [13]

2.2.5 Apertures

Wavefront shaping with the use of apertures is another way of manipulating a beam's amplitude and phase. By placing an aperture that is small enough in order to block undesired parts of the beam and let only certain parts of the wavefront to pass through. This method is deemed really difficult to be used because it requires a careful selection of the aperture that is going to be used to control the wavefront. Moreover, it provides little flexibility in the shape of the wavefront that it can produce but nonetheless, it is a really important method to be used in special cases [14].

Figure 2.9: Thorlabs Mounted Pinhole Aperture[15]

Another way of controlling the wavefront is by using annular apertures. These optical elements consist of a circular aperture with a central obstruction, creating a ring-shaped opening. By carefully adjusting the thickness, size, and position of an annular aperture we can transmit or block selectively the desired modes of light. These elements, as mentioned in other cases too, can be proven of great value

for correcting optical aberrations and manipulating the wavefront of a beam, and producing unique beam configurations [16].

Figure 2.10: Thorlabs Annular Aperture[17]

2.3 Gaussian Beams

In the field of Optics, a Gaussian beam is a particular form of a light beam whose intensity profile in the transverse plane can be defined by a Gaussian function[18]

$$I(r,z) = I_0(\frac{w_0}{w(z)})^2 exp(\frac{-2r^2}{w^2(z)}) \tag{2.6}$$

where w(z) is the radius of the Gaussian beam or the distance in the z-axis after which the intensity of the beam descends to $1/e^2$ of its maximum intensity value.W_0 is called the waist of the beam and it represents the minimum radius of the gaussian beam and r is the radial distance from the beam's center axis. The beam's radius is defined as follows [18]:

$$w(z) = w_0\sqrt{1+\left(\frac{z}{z_R}\right)^2} \tag{2.7}$$

where z is the distance from the waist along the z-axis, and $z_R = \pi w_0^2/\lambda$ is the Rayleigh range of the beam. The Rayleigh range represents the distance over which the beam remains approximately collimated before it starts to diverge. The width of the beam at z_R is $\sqrt{2}$ larger than the waist w_0 at the focus. The confocal parameter or depth of focus of the beam is defined as the distance between $-z_R$ and $+z_R$ [18].

If we define the total power of the beam as P_0, then:

$$I_0 = \frac{2P_0}{\pi w_0^2} \tag{2.8}$$

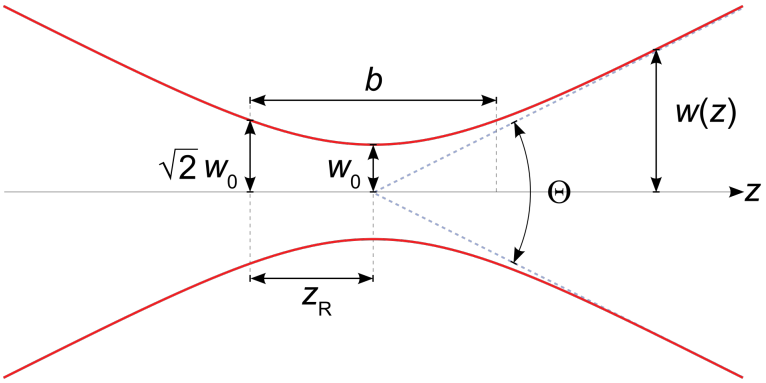

Figure 2.11: Gaussian beam diagram with parameters [19]

Gaussian beams are a key part of laser physics because the vast majority of all the beams produced by lasers are assumed to be almost perfect Gaussian beams. Their quality is defined by the M^2 factor which when is equal to 1, describes a perfect Gaussian beam. The factor that distinguishes those beams from other types is that when they pass through optical elements they retain their Gaussian form.[18]

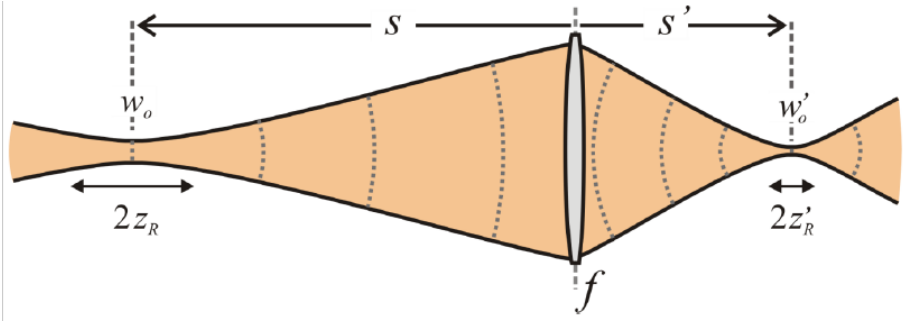

Figure 2.12: Gaussian beam through lens [20]

The mathematical description of a Gaussian beam when based on the wave equation in the paraxial approximation is given by:

$$\frac{\partial^2 E}{\partial x^2} + \frac{\partial^2 E}{\partial y^2} + 2ik\frac{\partial E}{\partial z} = 0, \tag{2.9}$$

where E(x,y,z) is the complex amplitude of the electric field, k is the wavenumber, and z is the propagation distance along the beam axis. This equation is subjected to many possible solutions that are essentially the different Transverse Electro Magnetic orders of the Guassian beam [18].

There are many possible Transverse Electro Magnetic orders but the most commonly laser-produced Gaussian beam is the fundamental or TEM_{00} mode [18].

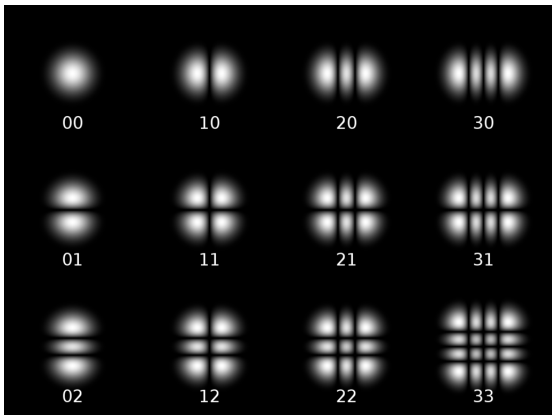

Figure 2.13: Spatial energy distribution for Hermite-Gaussian modes [21]

The complete expression for this lowest-order mode is given by the following equation which describes the complex amplitude of the electric field, split into 3 parts:

$$E(x,y,z) = E_0 \frac{w_0}{w(z)} exp[-\frac{r^2}{w^2(z)}] * exp[-i(kz - arctan(\frac{z}{z_0}))] * exp[-i\frac{kr^2}{2R(z)}] \tag{2.10}$$

The first part: $E_0 \frac{w_0}{w(z)} exp[-\frac{r^2}{w^2(z)}]$ is the amplitude factor, the second part: $exp[-i(kz - arctan(\frac{z}{z_0}))]$ is the longitudinal phase and the last part: $exp[-i\frac{kr^2}{2R(z)}]$ is the radial phase.[18]

2.4 Non Spreading Wavepackets - Non Diffracting Beams

Schrodinger's equation suggests that all wavepackets must alter their shape as they propagate in free space. In 1986, Balazs and Berry proved that some wavepackets do

not fall within this rule, without contradicting the physics behind it though. There is a family of beams that are called nondiffracting because they manage to retain their form as they propagate in free space for great distances. Airy Beams, Bessel Beams and Mathieu Beams appertain to this category. [22]

2.5 Airy Beams

Airy beams were the first type of non-diffracting beams that were theoretically demonstrated after proving that the Schrodinger equation for a free particle can provide an Airy wavepacket solution. The most astonishing feature of those beams is that they can accelerate without being subject to any kind of external field. The second exceptional feature is that they can turn as they propagate in free space. In other words we can say that they accelerate following parabolic trajectories while at the same time retaining their diffracting-free nature. [22] [23] Airy beams were first optically created and observed in 2007 by Georgios Siviloglou, John Broky, Aristide Dogariu, and Demetrios Christodoulides at the University of Central Florida. [23].

If we try to solve the normalized paraxial equation of diffraction, which is nothing more than the Schrodinger potential free equation, we can get a nondispersive solution.

$$i\frac{\partial \Phi}{\partial \xi} + \frac{1}{2}\frac{\partial^2 \Phi}{\partial s^2} = 0 \tag{2.11}$$

where Φ is the electric field, $\xi = z/kx_0^2$ is the normalized propagation distance , $s = x/x_0$ is a dimensionless transverse coordinate and $k = 2\pi n/\lambda_0$ is the wavenumber. The occurring accelerating Airy solution is the following:

$$\Phi(\xi, s) = \mathrm{Ai}(s - (\xi/2)^2)\exp(i(s\xi/2) - i(\xi^3/12)) \tag{2.12}$$

From the above solution, it is evident that the intensity profile remains unchanged after propagation while accelerating at the same time. The parabolic trajectory of

the Airy beam is described by the term $(\xi/2)^2$.

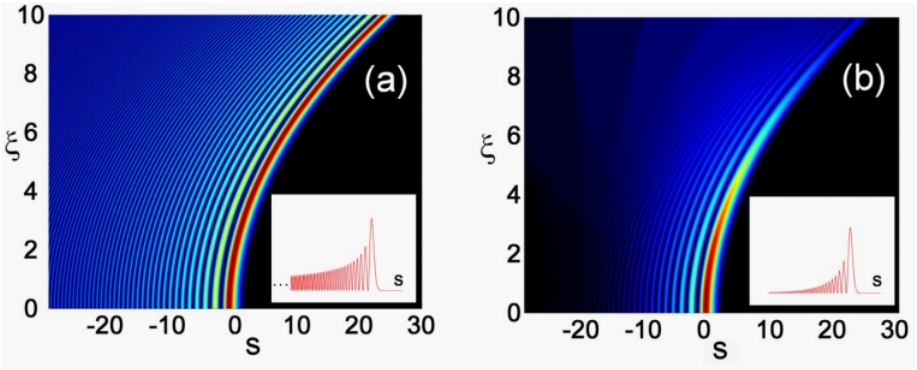

Figure 2.14: Propagation dynamics of (a) a diffraction-free Airy wave and (b) a finite-energy Airy packet [23]

The way of constructing such beams in real life was proposed by Siviloglou et Al.[23]. They found that the Fourier transform of the integrated equation 2.11 provides a solution that is proportional to the term $e^{ik^3/3}$ which essentially informs us that the angular Fourier transform of the Airy beam contains a cubic phase. Practically, this means that an Airy beam can be generated by a Fourier transform of a Gaussian beam while adding a cubic phase. An SLM which imposes a phase mask with cubic modulation can be utilized along with a converging cylindrical (1D) or spherical (2D) lens to provide the Airy beam[23].

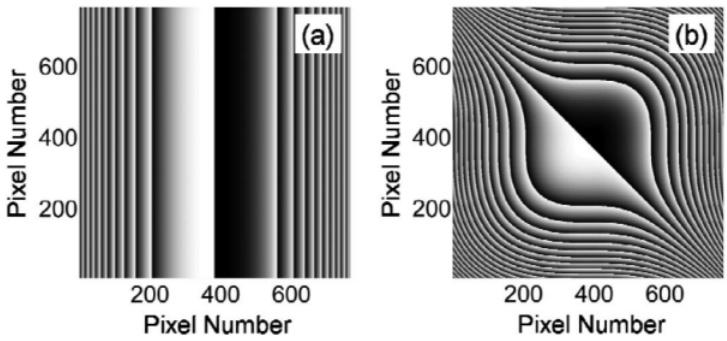

Figure 2.15: SLM phase masks used to generate (a) 1D and (b) 2D-Airy beams. Black color corresponds to 0 radians phase and white to 2π radians phase[23]

When comparing the non-diffracting properties of the Airy beam to the diffracting Gaussian beam we can claim that for distances that the Gaussian beam would have diffracted about 6-7 times, the Airy beam remains unchanged. As seen from Figure 2.16 the Airy beam retains its form for the same distance which its Gaussian counterpart has heavily diffracted [23].

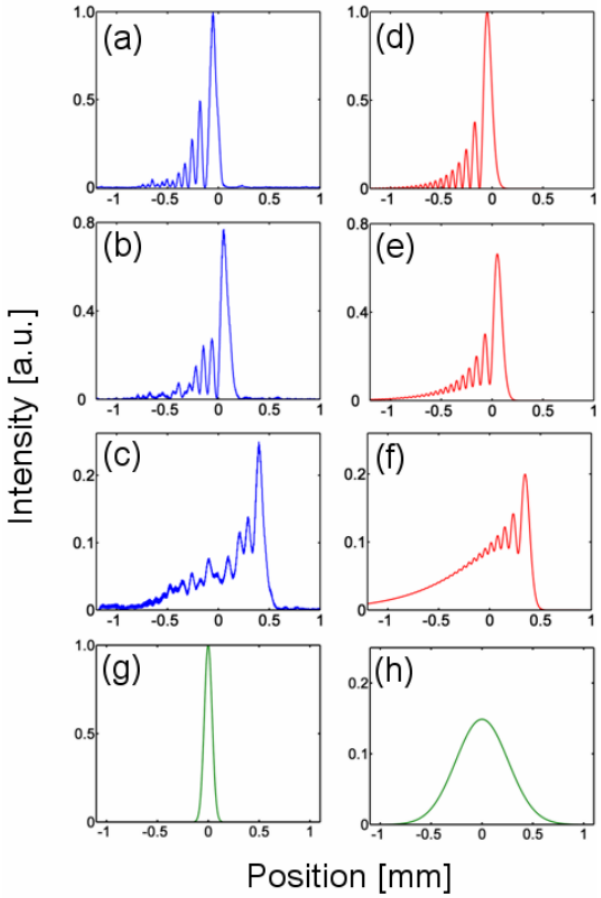

Figure 2.16: Observed intensity of a 1D Airy beam at (a) 0 cm, (b) 10 cm, and (c) 20 cm. Corresponding theoretical plots for these same distances (d)– (f). (g) A Gaussian beam having the same intensity FWHM as the first Airy lobe. (h) Corresponding diffraction profile after 25 cm of propagation[23]

.

2.6 Bessel Beams

Bessel Beams are another non-diffracting type of light beam with the unique feature to maintain their shape and intensity profile after propagating for a significant distance. This nondiffracting propagation distance can reach values of up to 17 times the rayleigh length of an equivalent Gaussian beam [24][25]. Moreover, its peak intensity oscillates about its initial value many times before collapsing to zero. This oscillation occurs primarily due to the diffraction produced by the edges of the various apparatuses used to produce such beams. We will expand on this matter further down this theoretical synopsis [24][25].

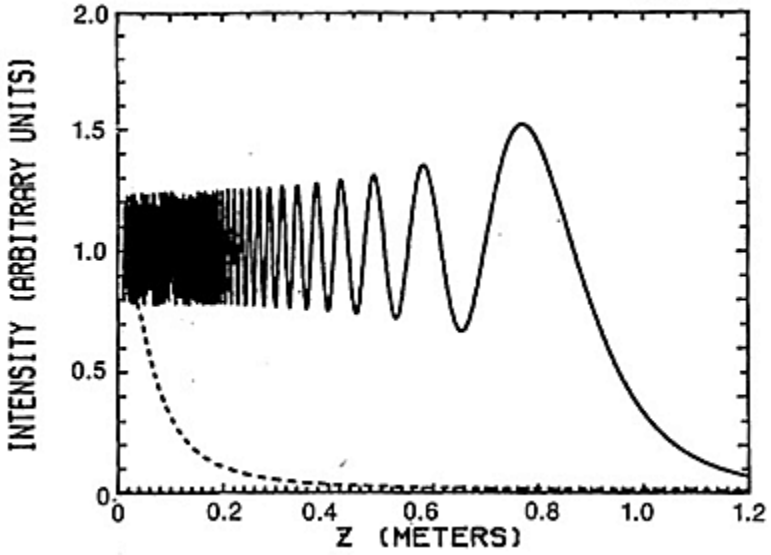

Figure 2.17: Intensities at beam center, as a function of distance. Zero-order Bessel beam (—) and Gaussian beam (- - - -)[25].

A Bessel beam is composed of a central maximum intensity spot and concentric ring-shaped maxima surrounding the central one. In theory, the number of concentric rings is infinite and the energy contained within each ring is the same. There is an arising problem with this theoretical approach though. Because the rings are infinite, this practically means that an infinite amount of energy would be required to construct a perfect Bessel beam. Obviously, this is not the case experimentally,

since an infinite number of rings cannot be produced. The number of rings that can be produced though, is limited by the means used to generate such a beam and the quality of the said means. We can generate Bessel Beams in a variety of ways[26]. There can be:

- Aperture Generated Bessel Beams
- Axicon Generated Bessel Beams
- Holographic Generated Bessel Beams
- Resonant Cavities Generated Bessel Beams

2.6.1 Aperture Generated Bessel Beams

A Bessel Beam can be constructed using an aperture by diffracting a laser beam through it and then focusing the diffracted beam with a lens. For this to happen, an annular slit should be placed at the focal plane of a lens. Since the Fourier transform of an annular slit is a Bessel beam, we can produce such beams this way. The mathematical proof is shown below: The intensity profile produced by an annular slit is given by:

$$I(x,y) = \begin{cases} 1, & a \leq x^2 + y^2 \leq b \\ 0, & \text{otherwise} \end{cases} \tag{2.13}$$

Here (x,y) are the spatial coordinates, a is the inner radius of the slit and b is the outer radius. The Fourier transform of this intensity profile is given by:

$$F(u,v) = \iint I(x,y)\ e^{(-2\pi i(u*x+v*y))} dx\ dy \tag{2.14}$$

Where (u,v) are the spatial frequencies in the Fourier domain. Evaluating this integral, we get:

$$F(u,v) = 2\pi \int_a^b \int_0^{2\pi} J_0(2\pi r\sqrt{u^2+v^2}) r\ dr d\theta \tag{2.15}$$

$$F(k) = 2\pi \int_a^b J_0(kr) r \, dr d\theta \tag{2.16}$$

Where J_0 is the Bessel function of the first kind, r is the radial coordinate in the spatial domain θ is the angular coordinate and $k = \sqrt{u^2 + v^2}$. Therefore, it has been shown that the Fourier transform of an annular slit is indeed a Bessel function. The order of the Bessel function is determined by the width of the slit, by carefully selecting the proper size of the slit it is possible to generate higher-order Bessel beams with more rings [26]. Practically, what happens is that this slit produces a converging conical wavefront, formed by a set of plane waves. The maximum theoretical propagation distance which the beam remains nondiffracting is given by the equation [24]:

$$Z_{max} = \frac{r_0}{tan(\theta)} = \frac{2\pi r_0 R}{\lambda}, \tag{2.17}$$

where r_0 is the aperture radius, θ is the angle of the conical wavefront with respect to the z-axis and R is the lens radius [27] [26] [24].

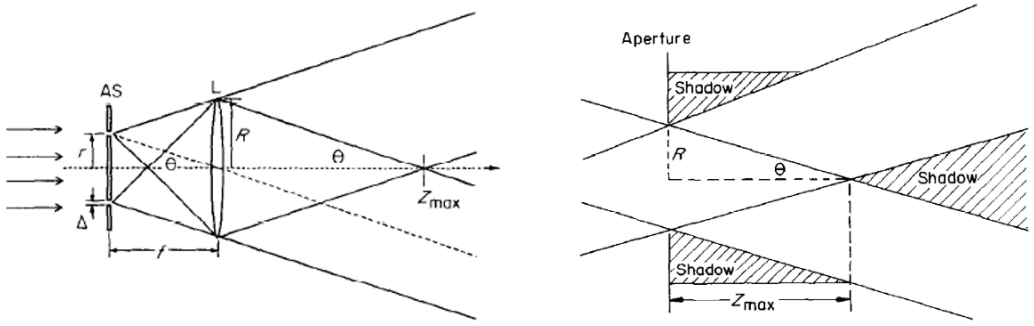

Figure 2.18: Left: BB produced by an aperture [26] Right: Zmax of an aperture generated BB [26]

.

2.6.2 Axicon Generated Bessel Beams

An axicon is a conical surface lens that can be used to produce Bessel beams. When illuminated by a Gaussian beam with waist size much smaller than the axicon's hard aperture it generates a conical wavefront. The refracted conical wavefront interacts

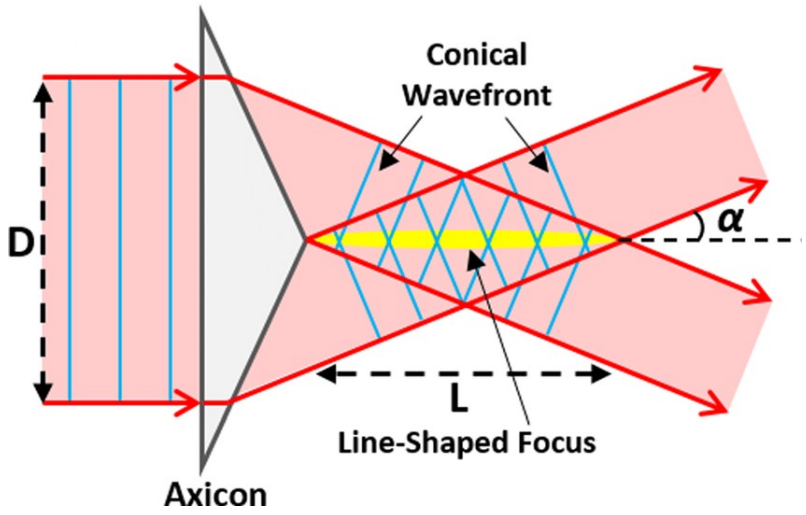

Figure 2.19: A BB generated by an axicon [28]

with itself and produces a Bessel Beam. This Bessel beam has nondiffracting properties within the Axicon's Depth of Focus given by the equation[26]:

$$Z_{max} = \frac{r}{(n-1)a}, \tag{2.18}$$

where r is the radius of the axicon, a is the angle of the axicon and n is the refractive index of the axicon. Beyond that point, a ring of an almost constant thickness (t) is produced[26],

$$t = \frac{r\sqrt{1-n^2 sin^2 a}}{cosa(nsin^2 a + cosa\sqrt{1-n^2 sin^2 a})} \approx r, \tag{2.19}$$

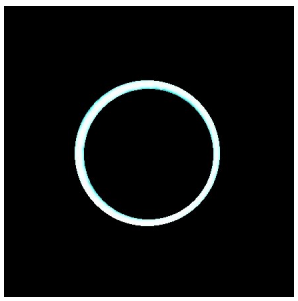

Figure 2.20: Bessel Ring of constant thickness t

2.6.3 *Holographic Generated Bessel Beams*

The use of static, etched holograms, or variable holograms produced by wavefront shaping devices can also be used to produce a Bessel beam of any order. The great advantage of using variable holograms is that it allows the user to produce Bessel beams of various orders and study their interactions with the experimental setup concurrently, without the change of any optical elements. This is useful if we need to manipulate immediately for any reason the shape of the Bessel Beam. The maximum propagation distance of such produced BBs is proportional to the Hologram radius (R) and the fringe spacing (r_0) [26]:

$$Z_{max} = \frac{2\pi r_0 R}{\lambda}. \tag{2.20}$$

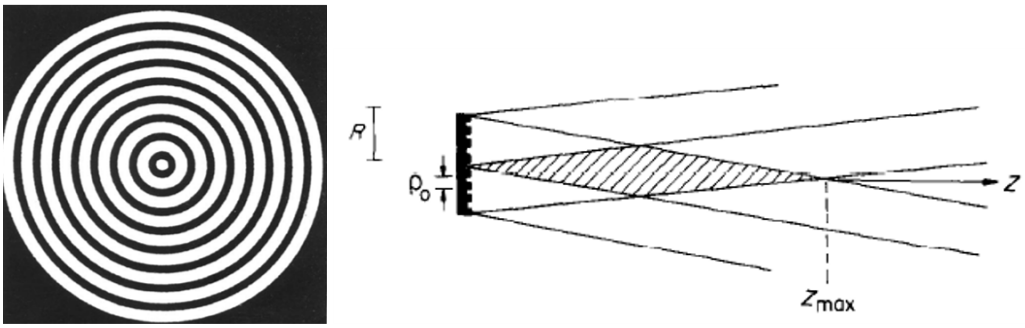

Figure 2.21: Left: hologram used to generate J_0 Bessel Beam distributions [26] Right: Holographically produced Bessel beam [26]

2.6.4 *Resonant Cavities Generated Bessel Beams*

A unique and quite intriguing way of generating a Bessel beam is via Resonant Cavities. What Indebetouw [29] first described theoretically was proven a few years later by Cox and Dibble [27].

When a spatially filtered laser beam passed through a pinhole it can be then considered a point source. This expanding Gaussian beam is then driven into a Fabry-Perot resonator, which has a fixed length d. The parallel rays arising from

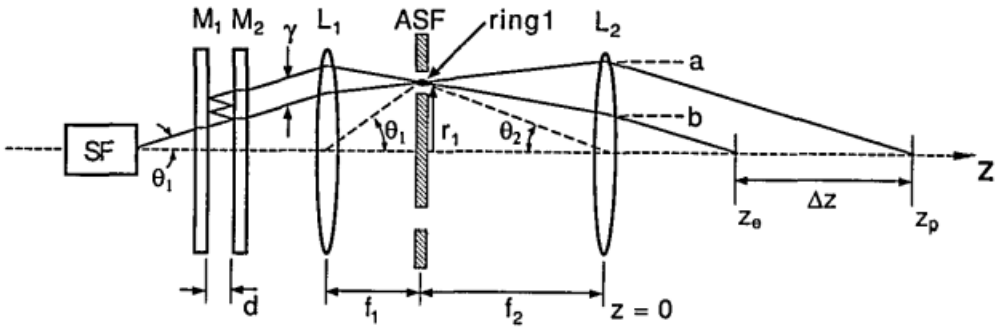

Figure 2.22: Diagram of the apparatus used for generating a BB via resonant cavities[27]

the Fabry-Perot resonator are then directed into the lens which focuses them and creates a Fabry-Perot ring pattern. With the use of an annular spatial filter, only one of the formed rings passes through and is then focused by a second lens, at a distance f, which creates the non-diffracting Bessel Beam pattern. Mathematically what we do is similar to the aforementioned method of the aperture-generated BB, since we select only a single spatial frequency with the filtering method and then Fourier transforming the occurring pattern with a single lens [27].

This method gives us a few fascinating results for the produced BB that are solely encountered in this way. Firstly, the diffraction-free distance occurring is equal to [27]:

$$Z_{max} = \frac{Fd}{\pi}, \tag{2.21}$$

where F is the cavity's reflectivity Finesse and d is the cavity length. By comparing this equation to the ones resulting from the other methods we can conclude that in this case, the diffraction-free distance is almost independent of the wavelength λ, contrary to the other cases, thus making the beam produced achromatic[27].

The second intriguing result is that the exhibited axial intensity oscillation is nonexistent in this case in contrast to the other methods. What occurs is that it grows until the point where it collapses to zero. This difference is considered to happen

due to the diffraction at the sharp edges of the apertures, axicons or holographic patterns while in this case, it is lacking[27].

2.7 Properties of a Bessel Beam

As mentioned before, a Bessel beam consists of successive bright and dark fringes (rings) thus making its intensity distribution sharply peaked. The envelope function which encloses the intensity distribution of a Bessel Beam decays at a rate inversely proportional to $a\rho$, where a is a constant and ρ is the distance from the center of the beam[26]. This practically means that the peak intensity of the concentric rings decreases at a rate inversely proportional to ρ [27].

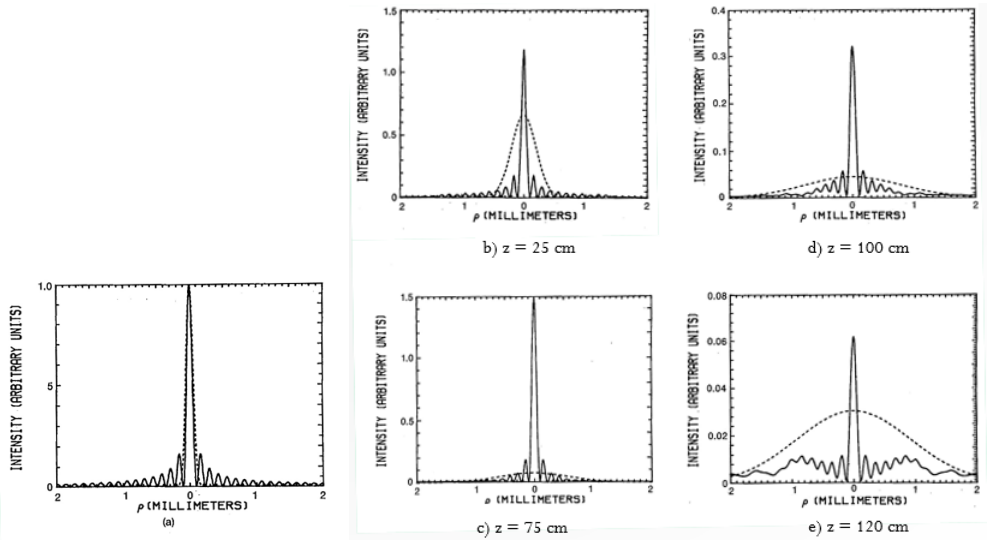

Figure 2.23: Intensity distributions for a zero-order Bessel beam (—) and a Gaussian beam (- - - -): (a) z = 0 cm.Note in (b)–(e) the intensity of the Gaussian beam has been multiplied by 10[25]

A Bessel beam has another unique and intriguing feature:a self-healing property. When this beam encounters an object, the waves that create the beam can move past the obstruction and recreate the intensity profile. The distance which this can be achieved after encountering the object is proportional to the size of the object. It has been shown that after blocking almost the whole beam we can get after a particular distance even 98.4% recovery of the initial intensity distribution. [30] This is evident

from the figures below that are based on the experiments on the self-healing part of the Bessel Beams which were conducted by Vetter et al. [30] When the beam was blocked by a screwdriver (yellow shape in Figure 2.24 (a)) and is strongly distorted (Figure 2.24 (b)), it can reinstate not only its original shape (98.4%) but also the majority of its peak power which remains at a value close to 96.9% of the unperturbed case [30].

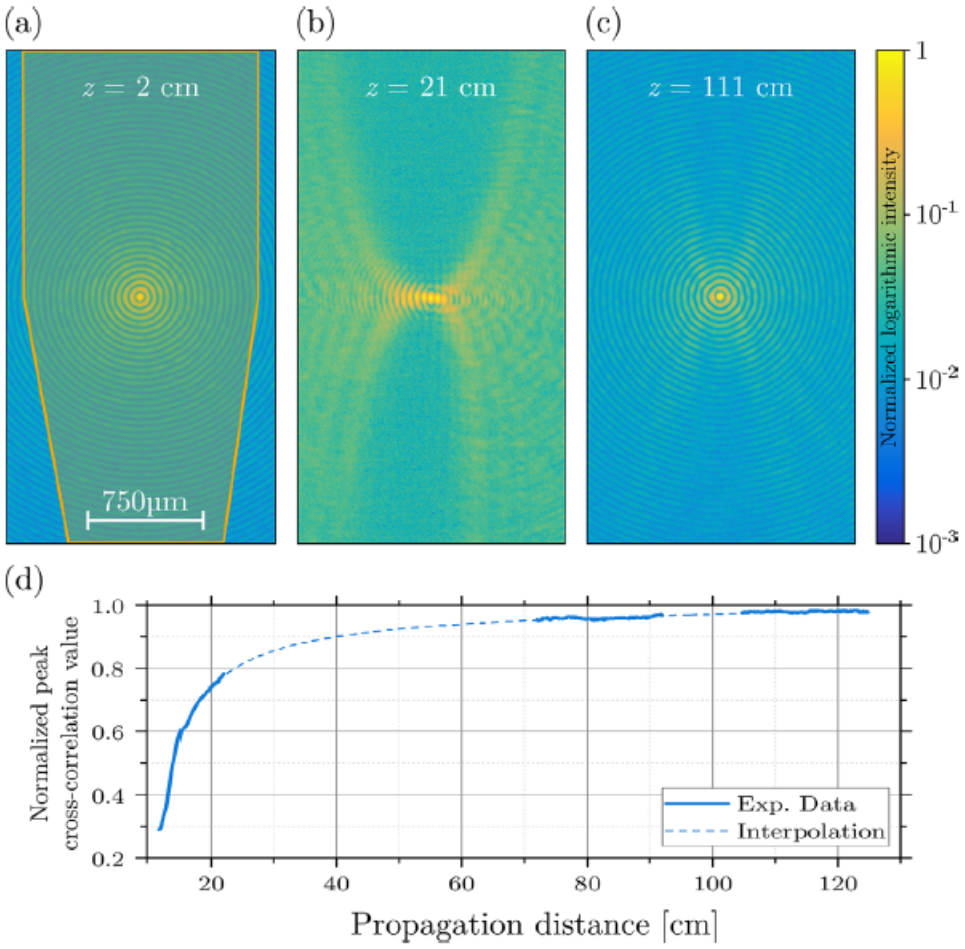

Figure 2.24: a) Sketch of the beam block and the initial Bessel Beam. b) Intensity distribution closely after the beam block. c) Intensity distribution after the beam self-healed. d) Cross-correlation between self-healing blocked Bessel beam and undistorted beam. [30]

2.8 Photoacoustic Imaging

One of the most aspiring and promising biomedical imaging techniques is photoacoustic imaging, gaining more and more attention in recent years. This imaging method is based on the photoacoustic effect. The basic principle of this effect is that when pulse radiation or time-variant radiation is delivered into the biological tissue being imaged, it generates a local rise in temperature. This heating leads to thermoelastic expansion of the tissue which causes ultrasound waves to be produced that can be detected by ultrasound transducers. By detecting and further analyzing those waves we can reconstruct a 3D image of the tissue. It is obvious that the contrast provided by this imaging method is caused by the differences in the absorption coefficients between the tissue elements [3].

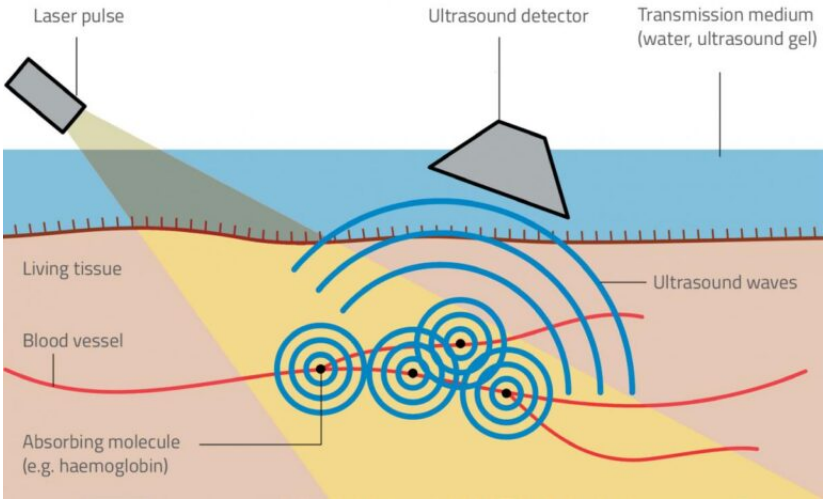

Figure 2.25: How photoacoustic imaging works [31]

Photoacoustic imaging is gaining more and more interest primarily because of its noninvasive nature. What that means is that it does not require any contrast agents or ionizing radiation to be utilized, therefore it is a patient-friendly examination process, unlike other alternatives such as X-ray imaging, CT scan, etc. Moreover, photoacoustic imaging can achieve high resolutions and contrast images when studying biological tissue. Lastly, since its contrast is based on the different

absorption properties of the various biological samples, it can be used to image functional processes such as blood flow which would be difficult to achieve with other methods[3].

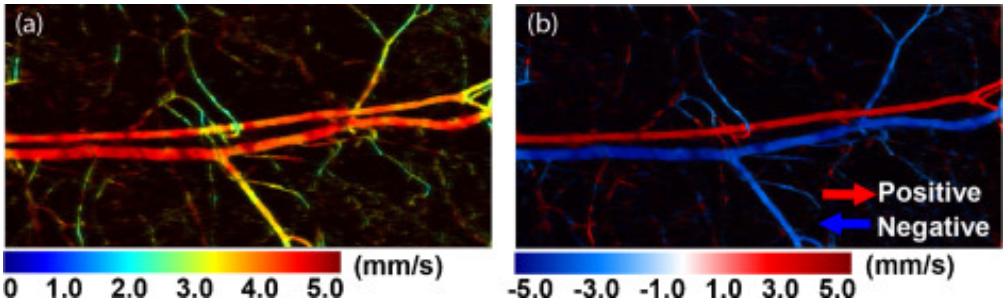

Figure 2.26: In Vivo Photoacoustic imaging of blood flow [32]

There are two parameters that are important in the mathematical description of photoacoustic imaging. The thermal relaxation time which is defined by equation 2.22 and is characteristic of thermal diffusion and the stress relaxation time which is given by equation 2.23 and is characteristic of pressure propagation[3].

$$\tau_{th} = \frac{d_c^2}{\alpha_{th}}, \tag{2.22}$$

where a_{th} is the thermal diffusivity and d_c is the characteristic dimension of the heated region

$$\tau_s = \frac{d_c}{v_s}, \tag{2.23}$$

where v_s is the speed of sound in the propagation medium[3].

For photoacoustic imaging, we need the laser pulse width to be smaller than both the thermal relaxation time and the stress relaxation time. When this happens it is said that the excitation is in stress and thermal confinement. Stress confinement is important because then the stress waves propagate only within the immediate region of interest while thermal confinement is important because that means that there is no thermal conductivity thus the heat generated remains confined to a small region around the target area, without spreading to neighboring regions[3].

As mentioned before, the local heating of an area by the laser pulse causes a volume expansion which is given by:

$$\frac{dV}{V} = -\kappa p + \beta T \tag{2.24}$$

By assuming stress and thermal confinement the volume expansion is considered negligible and the pressure right after the pulse is given by:

$$p_0 = \frac{\beta T}{\kappa} = \frac{\beta \eta_{th} A_e}{\kappa \rho C_v} = \Gamma \eta_{th} \mu_a F, \tag{2.25}$$

where Γ is the Grueneisen parameter

$$\Gamma = \frac{\beta}{\kappa \rho C_v} = \frac{\beta v_s^2}{C_P}, \tag{2.26}$$

μ_a is the optical absorption coefficient, η_{th} is the percentage that is converted to heat, A_e is the specific optical absorption and F is the optical fluence[3].

The following equation describes the generation of a photoacoustic wave in an inviscid medium:

$$(\nabla^2 - \frac{1}{v_s^2}\frac{\partial^2}{\partial t^2}) p(\overrightarrow{r}, t) = -\frac{\beta}{\kappa v_s^2}\frac{\partial^2 T(\overrightarrow{r}, t)}{\partial t^2}, \tag{2.27}$$

where $p(\overrightarrow{r}, t)$ is the acoustic pressure and $T(\overrightarrow{r}, t)$ is the temperature rise. By assuming thermal confinement this equation denotes:

$$\rho C_v \frac{\partial T(\overrightarrow{r}, t)}{\partial t} = H(\overrightarrow{r}, t) \tag{2.28}$$

By combining 2.27 and 2.28 we get:

$$(\nabla^2 - \frac{1}{v_s^2}\frac{\partial^2}{\partial t^2}) p(\overrightarrow{r}, t) = -\frac{\beta}{C_P}\frac{\partial H}{\partial t} \tag{2.29}$$

Here H is the heating function which is the thermal energy converted per unit volume and per unit time. Because 2.29 depends on the derivative of H, we can confirm

that we need time variant pulses in order to produce pressure waves and therefore acquire photoacoustic images[3].

Chapter 3

CREATION AND CHARACTERIZATION OF BESSEL BEAMS

3.1 Dedicated Experimental Setup

For our set of experiments, we utilized a variety of different experimental setups to accomplish the objectives we had set. In the first and most dedicated setup that we used, we managed to measure the characteristics of the produced Bessel Beam. The optical design included a Coherent Sapphire Continuous Wave Solid State laser with a wavelength of 488nm and an x16 telescopic system that magnified the diameter of the exiting laser beam in order to overfill the 1-degree axicon that was used to produce the Bessel Beam. Lastly, a plano-convex lens was placed one focal length away from the axicon's focus, creating the Bessel Ring, right at the entrance pupil of a x10 Meiji objective with NA=0.2 that was used to focus the beam. The ring's diameter was slightly smaller than the entrance pupil of the objective. The detection system, which provided the necessary resolution for the beam characterization, comprised of a Point Grey CCD camera and a Mitutoyo Plan Apo x50 objective. This dedicated setup was the springboard to more complicated ones that we will expand on further in this thesis.

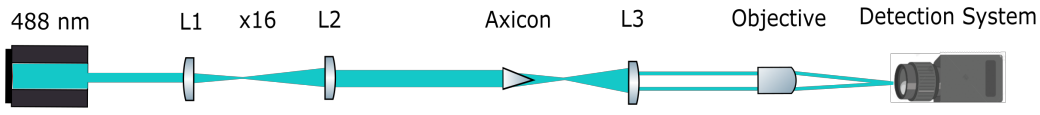

Figure 3.1: Setup for Bessel Generation

3.2 Bessel Beam Characterization

Our initial steps were towards characterizing the properties of the generated Bessel Beam. Parallel to building this experimental setup, we run simulations with equivalent optical parameters that were mentioned in the previous section for the experimental design. The simulated results provided an intuition of what approximately the beam will look like in terms of depth of field, FWHM, and Intensity profile. We chose carefully these values in order to produce a beam with a depth of field of approximately 1 mm. The thought process behind this choice was that the transducer that was going to be used for photoacoustic imaging, later on, has a detection depth of 1mm, so we wanted to create a Bessel beam that would retain its profile almost unchanged for about the same length. This way we would be able to exploit to the greatest degree the detection depth of the transducer.

Upon completing the experimental setup, we captured images of the Bessel Beam at various distances along the z-axis. Moreover, after data processing, we were able to produce graphs about the beam's FWHM and its intensity profile. As we can see from the figure below (Figure 3.2), the produced Bessel has a central maximum intensity spot and concentric ring-shaped maxima surrounding it as expected from the theory.

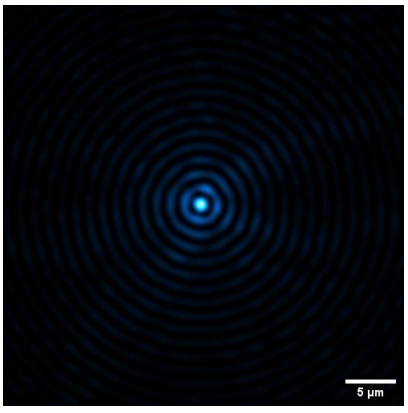

Figure 3.2: Bessel Beam created by the dedicated setup

To construct the figure below, which depicts the Bessel Beam along the z-axis, we captured a sequence of images by moving the detection system along the propagation axis, with a step of 100 μm, and with the use of ImageJ we managed to reconstruct the image of the Beam. When comparing Figures 3.3 and 3.4, we can see the apparent resemblance of the simulated and the generated Bessel beam along the propagation axis as long as the r axis. Regarding the depth of field, the generated beam coincides with the beam that resulted from the simulation methods. Taking a close look at the two figures below and comparing them we can safely reach the conclusion that both beams have a Depth of Field of approximately 1 mm.

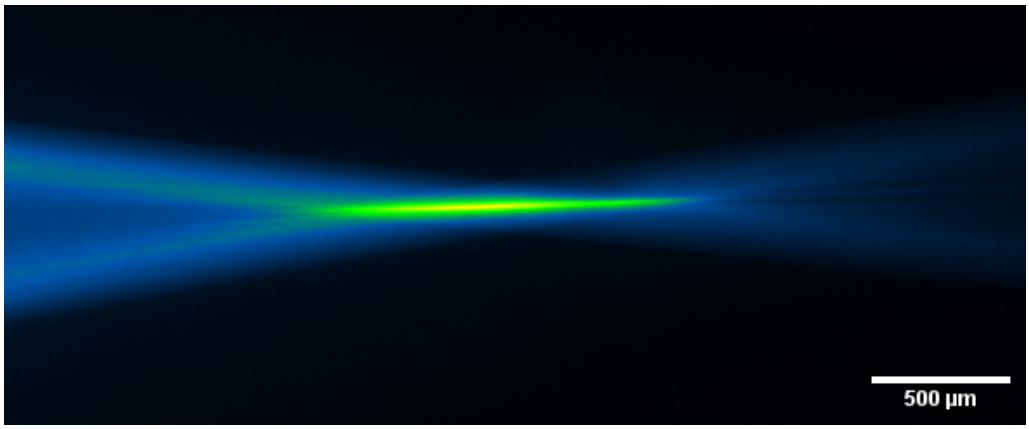

Figure 3.3: Bessel Beam along z-axis

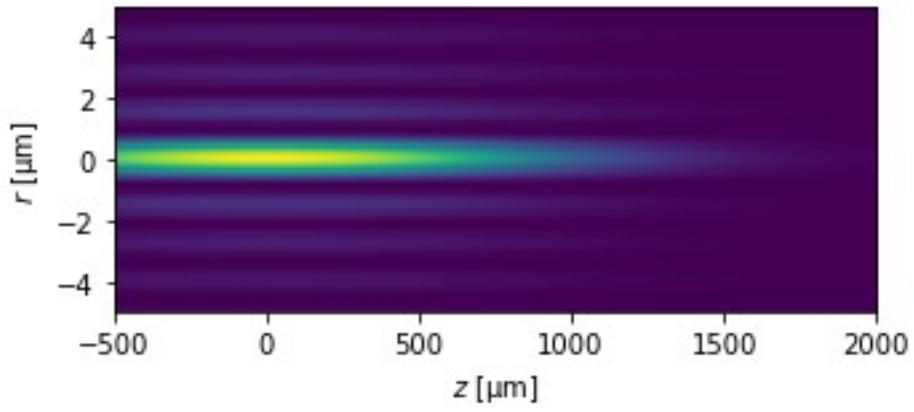

Figure 3.4: Simulated Bessel Beam along z-axis

This conclusion is apparent for the simulated one by the scaling of the image, while for the generated Bessel Beam becomes apparent upon looking at Figure 3.5. In this graph we can see that the FWHM retains its value for approximately 1 mm along the z-axis, therefore the DOF of the beam is almost 1mm.

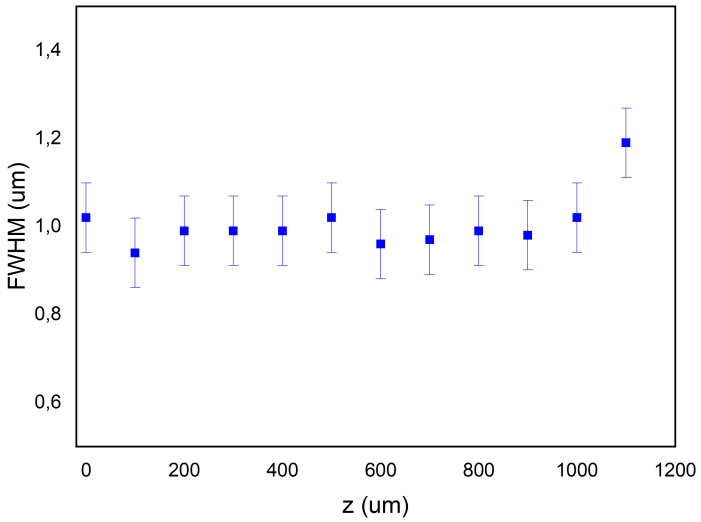

Figure 3.5: FWHM of Bessel Beam

We can further provide a comparison of the Intensity profile for the Bessel Beam. Once again, Figure 3.6 is a graph that depicts the results that emerged from the simulation for the intensity profile of the beam, and as we can see when comparing them with Figure 3.7 which is constructed using experimental data, we can observe many similarities. The normalized intensity of the first side lobe barely reaches the value of 0.25 for both graphs while the second and third lobes are close to 0.12-0.14 respectively. Moreover, the diameter of the central lobe, minimum to minimum is about 2mm for both graphs (FWHM=1mm). The only part where we have a slight mismatch is the frequency of the side lobes which appears to be infinitesimal lower in the case of the experimental results. This may be attributed due to slightly different values in the optical elements used in the actual setup in comparison with the simulated values for the optical elements. Lastly, even though

we were generally satisfied with the generated Bessel Beam, we could spot another minor problem with the intensity Figure. The problem is that the symmetry is not perfect in terms of intensity for the side lobes. This may be addressed by altering the tilt in the axicon or some other optical element.

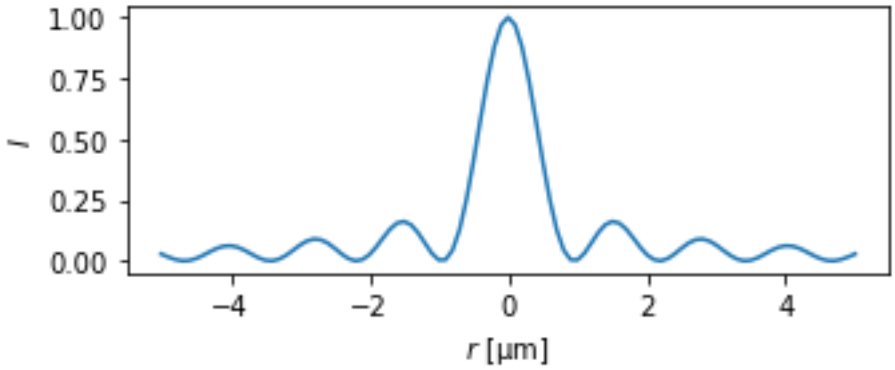

Figure 3.6: Bessel Beam Simulated Intensity Profile

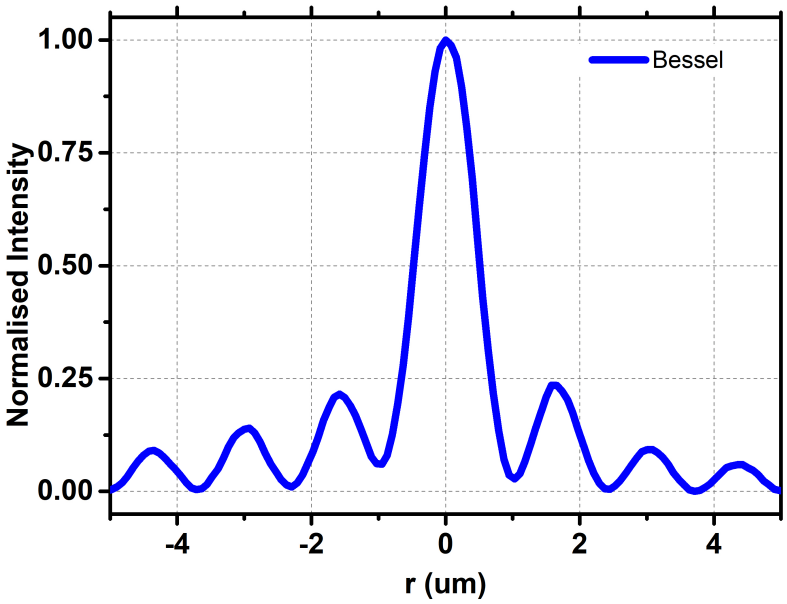

Figure 3.7: Bessel Beam Measured Intensity Profile

3.3 Scattering Effect on Bessel Beams

In this part of the experimental process, we tried to obtain some information about the scattering properties of the Bessel Beam and compare those properties with the Gaussian Beam. To do so, it was necessary to construct a medium through which the beam was going to propagate. We decided that this medium was going to be TiO_2 dissolved in Gel Wax, in different concentrations, which has been used extensively in the bibliography as a scattering medium. This mixture was placed on aluminum slabs and was fixed in place with the use of two very thin microscope coverslips. These slabs were placed between the two objectives, so the beam would pass through them, be subjected to scattering, and be detected by the detection system.

The Reflectivity (R) and Transmissivity (T) values for the different slabs were measured with the use of a spectrophotometer between 478 and 498 nanometers wavelength. With the use of these measured values, we were able to determine with high accuracy the scattering properties of each slab. To do so, we utilized the Software developed by Scott Prahl [33] which provided the corresponding reduced scattering coefficient for each set of R and T values. The reduced scattering coefficient is a parameter that quantifies the probability of scattering events occurring in a medium and it is the reciprocal value of the mean free path.

After characterizing the scattering slabs, we set them in the experimental setup as described before and as shown in Figure 3.8. Then we captured images at the focus for all the slabs available for both the Bessel and the Gaussian beams.

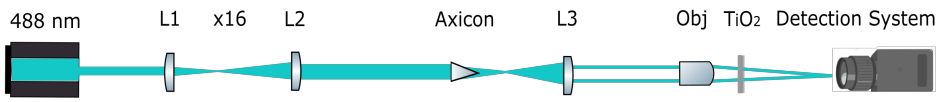

Figure 3.8: Setup for scattering measurements

An obvious conclusion derived from a first inspection of the captured images is that the Bessel Beam just like the Gaussian one retains its shape and intensity

almost completely for Reduced Scattering Coefficient (RSC) values ranging from 0 to approximately 3 cm^{-1} as can be seen from the images below.

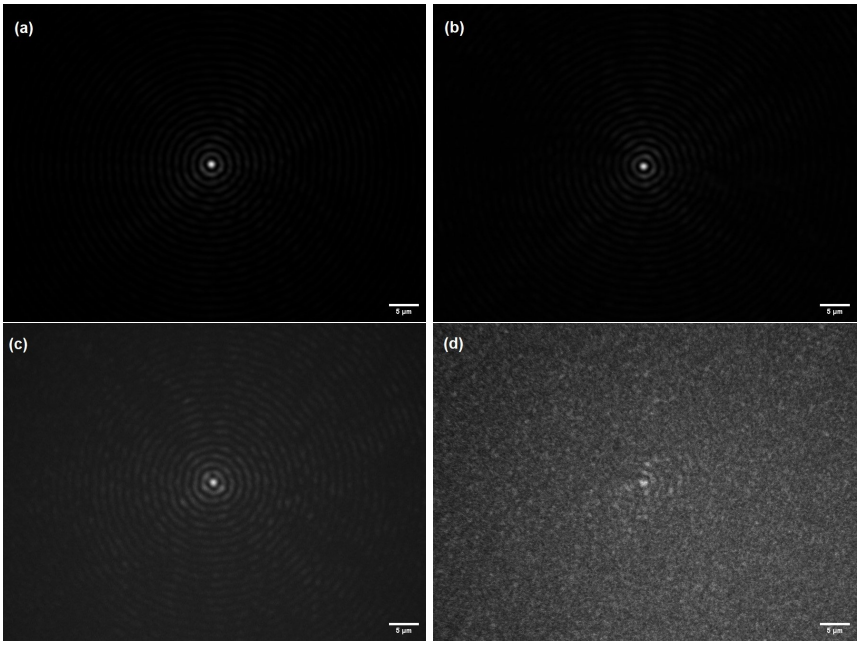

Figure 3.9: Scattering on Bessel Beam for (a) RSC=0, (b) RSC=2.1, (c) RSC=3.8, (d) RSC=5.7

For Reduced Scattering Coefficients greater than approximately 3 cm^{-1} scattering affects both beams a lot but most importantly it affects the Bessel Beam. We can attempt to make a leap further and quantify the effect of scattering by calculating the Full Width at Half Maximum (FWHM), the Signal to Background Ratio (SBR), and the Inhomogeneity for each image using the following formulas:

$$FWHM = \Delta x|_{ymax} \tag{3.1}$$

$$SBR = \frac{Mean_{center}}{SD_{background}} \tag{3.2}$$

$$Inhomogeneity = \frac{SD_{center}}{Mean_{center}}, \tag{3.3}$$

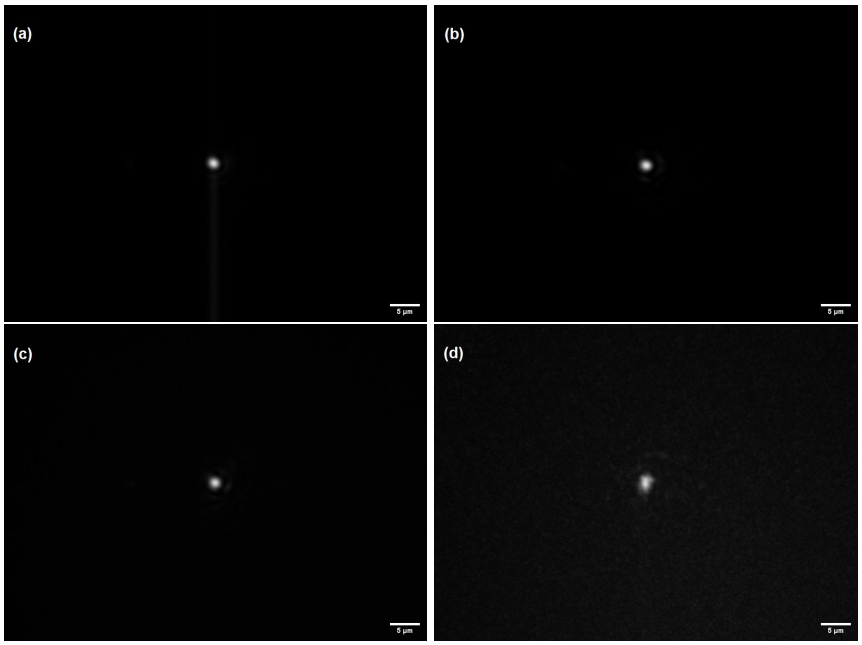

Figure 3.10: Scattering on Gaussian Beam for (a) RSC=0, (b) RSC=2.1, (c) RSC=3.8, (d) RSC=5.7

where SD: Standard Deviation. In order to calculate those values we set a circular area with a diameter of approximately the FWHM value, inside the central maximum of the Bessel Beam or the Gaussian one, to extract the values for $Mean_{center}$ and SD_{center} and really far away from that central spot ($\approx 10-20FWHM$) to extract the values for $Mean_{background}$ and $SD_{background}$. After calculating the aforementioned parameters, we plotted the occurring values against the Reduced Scattering Coefficient values of the scattering slabs and produced the following figures.

As we can see from Figure 3.11, both Bessel and Gaussian FWHMs are almost constant for lower RSC values. As we increase the coefficient, scattering impacts more and more the FWHM of the beams and starts to grow exponentially. The dependence of FWHM on the reduced scattering coefficient is greater for the Bessel, as it loses its initial value more abruptly than the Gaussian one. This is to be expected as the BB has a more complex intensity distribution than the Gaussian one

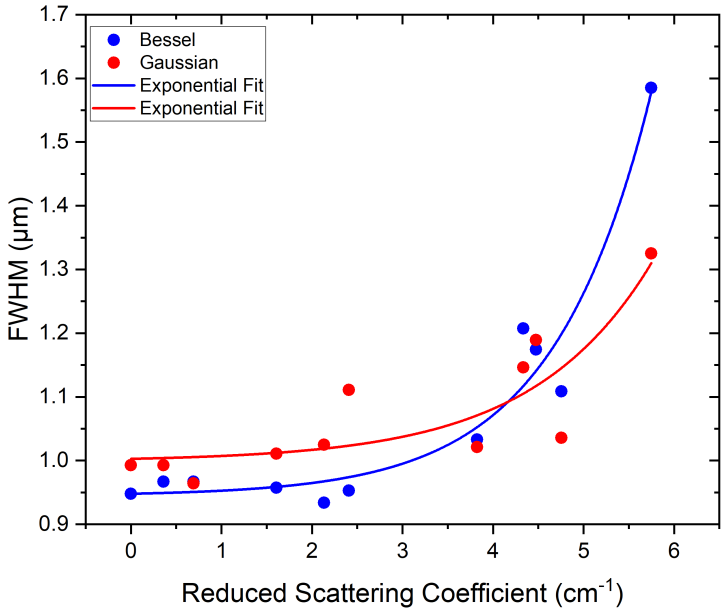

Figure 3.11: FWHM vs RSC Scattering Slabs

and consequently, scattering produces interference between the concentric rings and therefore disturbs the intensity distribution much more. The R-squared for the Bessel Beam is 94.7 while for the Gaussian Beam is 73.7.

In the matter of the Signal-to-Background Ratio, we use a semi-logarithmic scale and we provide a linear fitting for both the data sets for both beams. As we can observe SBR falls more abruptly for the case of the Bessel Beam than the Gaussian one, as seen clearly by the mere visual inspection of Figures 3.9 and 3.10. The R-squared values for these fittings are 95.8 and 89.8 for the Bessel and the Gaussian Beam respectively.

The metric exhibiting a strong variation between the two beams is Inhomogeneity which describes how inhomogeneous is the beam. While the Bessel Beam starts at lower values in comparison with the Gaussian one it quickly surpasses its Gaussian counterpart and increases linearly while the Inhomogeneity for GB stays almost undisturbed.

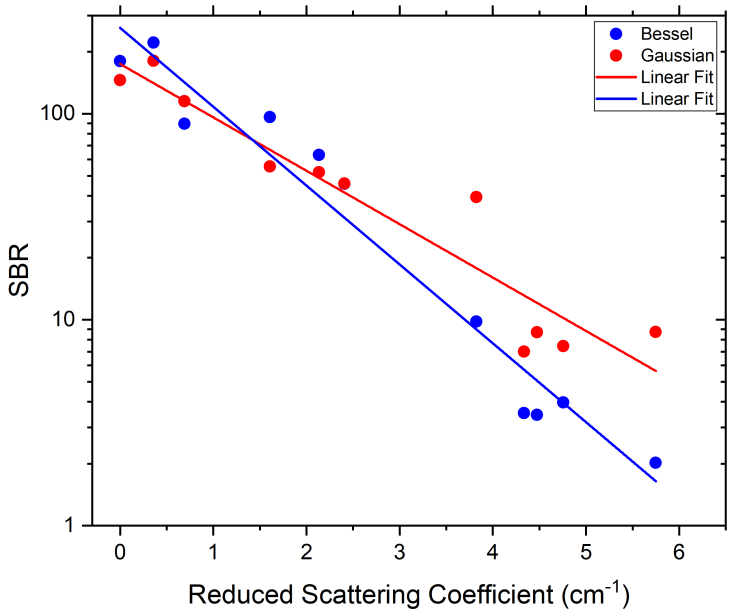

Figure 3.12: SBR vs RSC Scattering Slabs

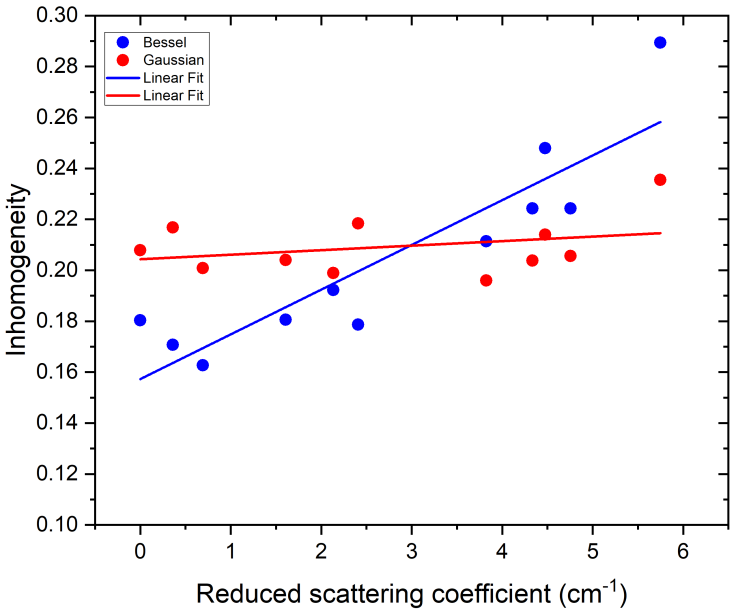

Figure 3.13: Inhomogeneity vs RSC Scattering Slabs

3.4 Droplet Beam

As mentioned earlier, our initial course of action was to generate a Bessel Beam, suppress its side lobes, and produce a new beam that is often referred to as a Droplet

Beam [2]. In this paper[2] published by Di Domenico in 2018, they project a mask of two concentric rings on a Spatial Light Modulator in order to produce two different Bessel Beams and due to the interference of those two beams to diminish the peripheral rings of the final Bessel beam. The level of suppression, in this case, is dictated by the ratio of the diameters of the two rings that are projected. The problem with this method is that the cost of a SLM is really high and most importantly a great portion of the incident to the SLM energy, about 98%, is going to waste in order to project only those two rings. In our case, we came up with an ingenious alternative way of producing this droplet beam without using a Spatial Light Modulator. To achieve this we developed and utilized the experimental setup shown in Figure 3.14, which is essentially a variation of a Mach-Zender interferometer.

The beam arising from the 488nm laser is magnified by an x16 telescopic system and is filling the axicon which transforms it into a Bessel Beam. Then, a non-polarising beam splitter splits the BB into two parts, with each part receiving 50 percent of the initial power. Two plano-convex lenses L3 and L4 are placed at distances f3 and f4 at the short and long "arm" of the interferometer respectively and are creating a different-sized Bessel ring each. Finally, a second non-polarising beam splitter combines the two beams into a common path toward the focusing Meiji Objective.

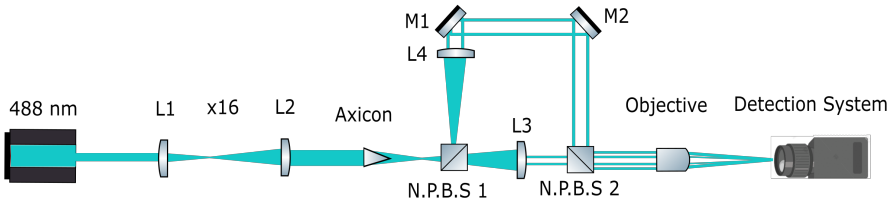

Figure 3.14: Setup for BB side lobe suppression

Essentially what we do in this setup is that we generate two different Bessel Beams with the use of the two different lenses at different paths and then the interference of those two beams is producing the Droplet Beam. An important aspect of this interferometer is that in each arm because the lenses have different

focal lengths they create Bessel rings of different diameters. As claimed before, the ratio of the diameters of those rings is defining essentially if we will be able to create the aforementioned Droplet Beam. When the ratio is between 0.4 and 0.8, the suppression of the Side lobes will be the greatest as claimed by Di Domenico [2]. So initially, we needed to decide the focal lengths of the two lenses that would create the Bessel Beams. To achieve this, we used simulation to see the produced intensity profile of the two beams for different combinations of lenses. The two possible combinations that would produce adequate results were f1=1000mm and f2=500mm and f1=1000mm and f2=750mm. The simulated results are shown in the following figures:

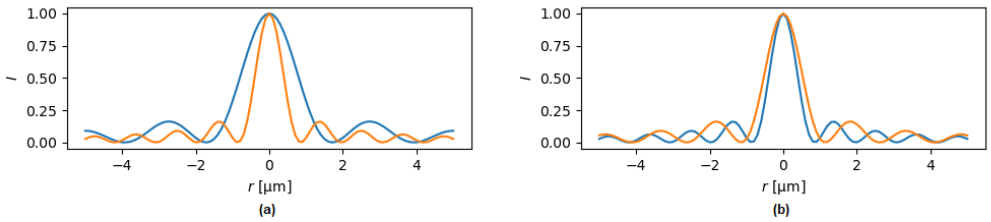

Figure 3.15: Simulated results for (a) 500-1000mm interference and (b) 750-1000 mm interference

As we can easily observe from the simulated intensity profiles for the two combinations of lenses, the overlap of the two individual intensities is far greater for the second combination than the first one, so our intuition was that we would achieve a greater side lobe suppression for the second case.

After setting up our setup with those two different combinations, we once again captured images that are shown in the next Figures.

From these images, we produced the intensity profile of each of them and after normalizing the intensities and centering the occurring maximum value we got the following Figures:

If we compare those figures with the simulated one we can conclude that they generally have a good correlation. There are two arising problems. The first one

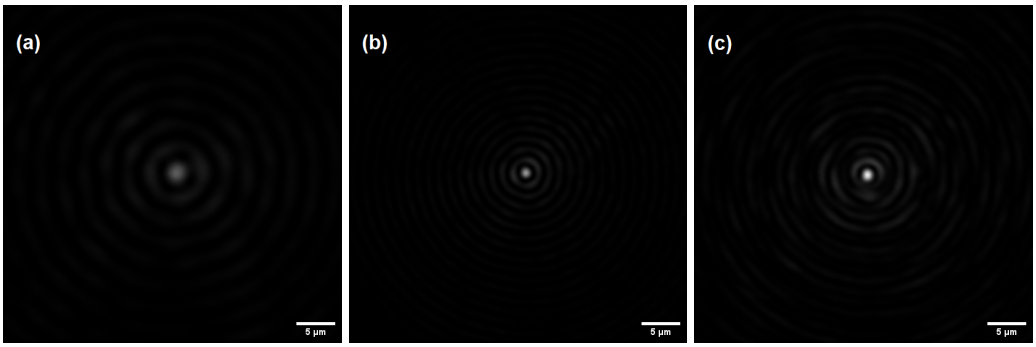

Figure 3.16: Bessel Beam produced by (a) 500mm lens, (b) 1000mm lens, and (c) Interference

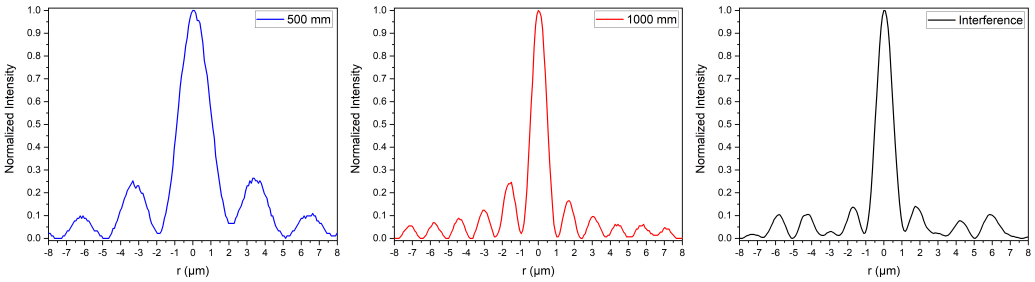

Figure 3.17: Intensity Profile (a) 500mm lens, (b) 1000mm lens, and (c) Interference

is that for the 1000mm arm we can see that there is some kind of tilt in the lens that produces a non-symmetrical Intensity profile. The second and most important problem with this lens combination is that the interference intensity profile produced shows second lobe suppression only. This comes as no surprise if we observe the simulated intensity profile carefully. Therefore, the second set of lenses should improve the suppression of side lobs and produce a more suitable Droplet beam. Consequently, we advert to the 750mm and 1000mm combination for better results. We once again captured images of the two individual beams and their interference which are shown below.

As before we took the intensity profiles for the above images and the results are shown below.

Comparing the two cases of interference we can easily see that this second case

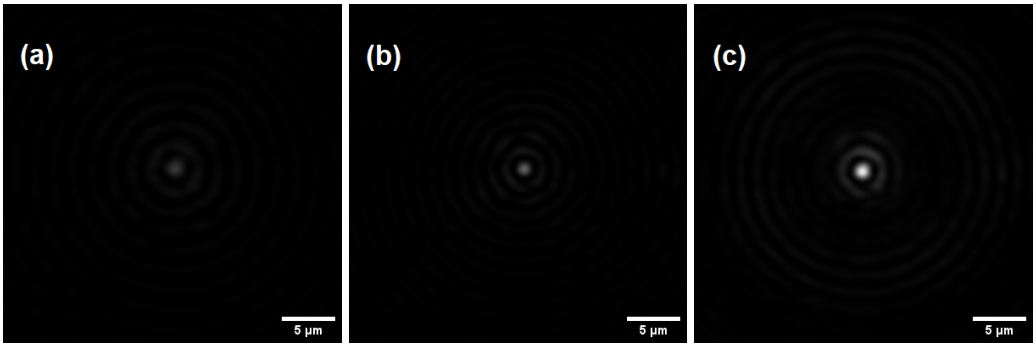

Figure 3.18: Bessel Beam produced by (a) 750mm lens, (b) 1000mm lens, and (c) Interference

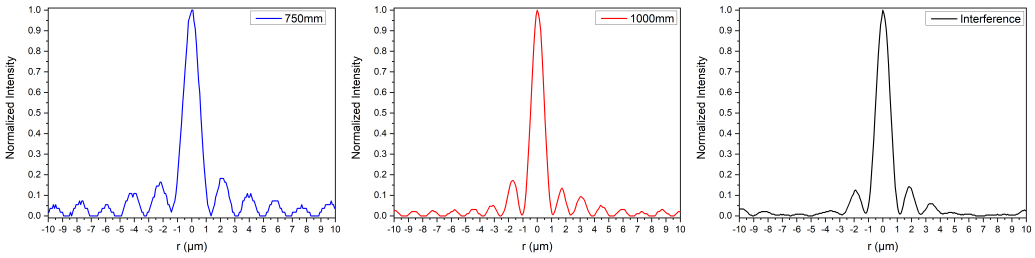

Figure 3.19: Intensity Profile (a) 750mm lens, (b) 1000mm lens, and (c) Interference

is much closer to our goal. More precisely, the interference produced shows a complete suppression of all the concentric rings that are reduced to background levels, except for the first ring which retains an intensity of about 12-14 % of the central maximum. Even though this value is not suppressed as the other ones, it still shows a reduction in comparison with the two individual Bessel Beams, in which the intensity is 15-20 % of the maximum intensity. In conclusion, this setup produced promising results and was able to produce a Droplet Beam. From the analysis of both these cases, we managed to prove the claim of Di Domenico [2], in which he argues that the ratio of the two rings produced by the lenses determines the level of suppression that can be achieved.

Chapter 4

MULTIPARAMETRIC MICROSCOPE

4.1 Photoacoustic Imaging with Transmission Geometry Microscope

Before proceeding to the integration of the Droplet beam in our multiparametric microscope, we tried to acquire photoacoustic images with an already existing photoacoustic imaging setup. By acquiring those images we wanted to investigate if the extended Depth of Field of the Bessel beam can provide constant image resolution for greater distances compared to the Gaussian beam case. This photoacoustic imaging setup utilizes transmission geometry. This means that the sample is radiated from the bottom and the ultrasound waves that are produced are detected from the top of the sample as seen in the experimental setup in Figure 4.1

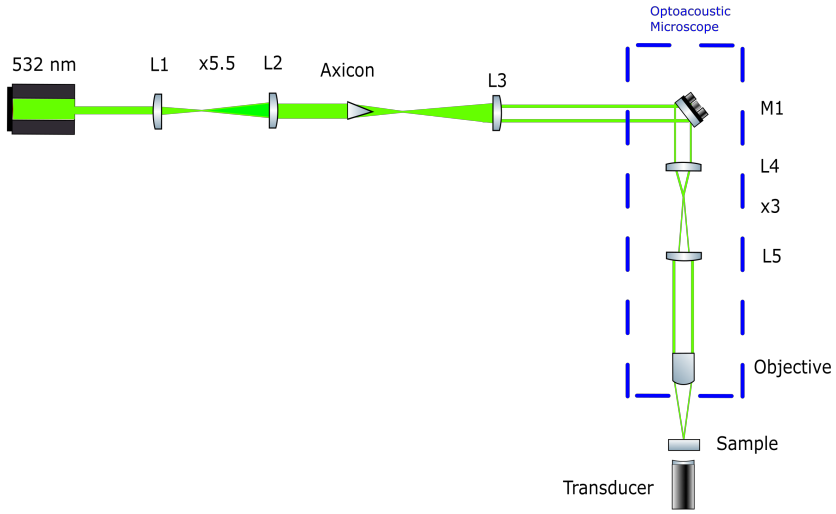

Figure 4.1: Setup for Photoacoustic Imaging with Transmission Geometry Microscope

The photoacoustic images shown in Figure 4.2 were taken with the aforementioned optoacoustic microscope setup for two different beam cases. With a Gaussian beam and a Bessel beam along with all the peripheral rings. Note here that this is

not a Droplet Beam. As an imaging phantom, we used two carbon rods forming a crosshair. The vertical rod is on top and the horizontal one is on the bottom. Each rod had a diameter of about 500 μm. For both images, we focused on the middle of the bottom rod. From a quick observation of Figures 4.2 (a) and (b) we can clearly see that the Bessel Beam image retains its resolution constant for greater distances as we can see both rods simultaneously in focus, while for the case of the Gaussian beam, we can only see the bottom rod in focus. Moreover, in the case of the Bessel Beam, we can distinguish the limits of both rods when in the case of its Gaussian counterpart, the outer limits of the top rod are completely lost. All these results are attributed to the much-extended DOF of the Bessel Beam, which in this case is about 1mm.

A significant problem arising from the image acquisition process was that in order to obtain the image with the Bessel Beam we were forced to use about double the power of the one we used for the Gaussian case. Obviously, this is a heavy burden since our end goal is to use photoacoustic imaging for biological samples. Therefore in order to drop the necessary power significantly without losing the extended DOF of the Bessel beam it was necessary to integrate the Droplet Beam, at a photoacoustic imaging setup.

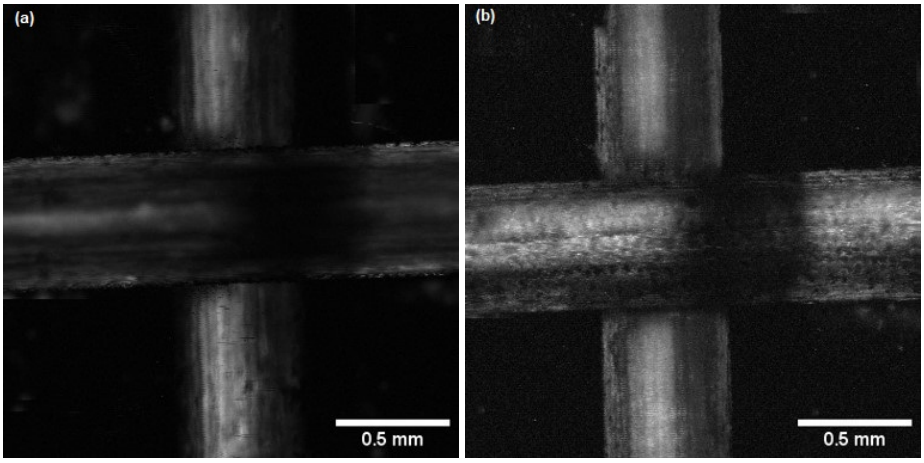

Figure 4.2: Carbon rods Photoacoustic Imaging with (a) Gaussian Beam, (b) Bessel Beam

4.2 Integration of Droplet Beam

Having seen promising results from the level of suppression achieved by the creation of the Droplet Beam we set a new goal: To integrate the previous setup of the interferometer into a Multiparametric microscope that utilizes 3 different imaging methods. This task proved to be extremely difficult because we had to align laser beams of both infrared and visual wavelengths through the same optical elements. We were also obliged to make new simulations and calculations for the appropriate combination of lenses that would be used in the Mach-Zender interferometer because in this setup we use a pulsed 532 nm Coherent laser instead of the CW Coherent Sapphire 488 nm laser of the previous setup. Also, because there is an x2 telescopic system built into the optoacoustic microscope, even if the wavelength stayed the same, we would have to change the combination of lenses. All in all, we constructed the same Mach-Zender interferometer setup with a different combination of lenses and attached it to the Optoacoustic Microscope's entrance. The main difference is that we did not image the two Bessel rings directly at the entrance pupil of the focusing objective but at Galvo mirrors so that we can scan our sample much faster.

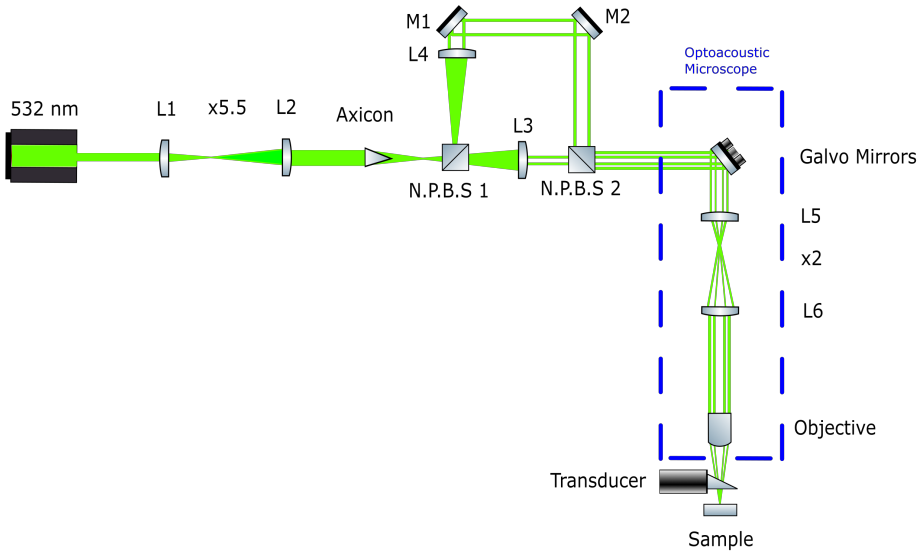

Figure 4.3: Setup for Photoacoustic Imaging with Droplet Beam

4.3 Photoacoustic Imaging with Reflection Geometry Microscope

The photoacoustic imaging setup is shown in Figure 4.3 and utilizes reflection Geometry which means that the sample is radiated from the top and the ultrasound waves that are produced are detected by a transducer that is on top of the sample too. The main advantage of using a reflection geometry photoacoustic imaging setup is that we can acquire images of much larger samples because we are not limited by the thickness of the sample. On the other side, in order to utilize this reflection geometry we have to sacrifice a part of the image resolution and sensitivity compared with the transmission geometry setup. The decrease in the resolution and sensitivity is attributed to mechanical reasons that limit us in the case of the reflection geometry setup. Since the transducer should be placed directly between the sample and the focusing objective this forces us to use objectives with smaller numerical aperture values which imperatively lowers the resolution of the whole microscope. Moreover, because the reflection geometry requires the spatial separation of the excitation optical beam from the detected acoustic beam, the acoustic-optical beamsplitter or an off-axis transducer which are utilized, are introducing losses to the recorded signal. In order to compare the DOF for 3 different beam cases (Gaussian Beam, Bessel Beam, and Droplet Beam) we managed to obtain three different photoacoustic images. As an imaging phantom, we used a 45-degree prism with black tape on its hypotenuse. The focus was set at approximately the middle of the hypotenuse of the prism and we took the following three images for the three different cases.

From a mere optical observation and comparison of the three images, we can see that indeed the aforementioned claim, that the DOF is much greater for the cases of the Bessel Beam and the Droplet Beam than their Gaussian counterpart stands completely true. A number juxtaposition affirms this claim too, as the DOF of the Gaussian is $\approx 1100\mu m$, for the Bessel Beam $\approx 2600\mu m$, and for the Droplet

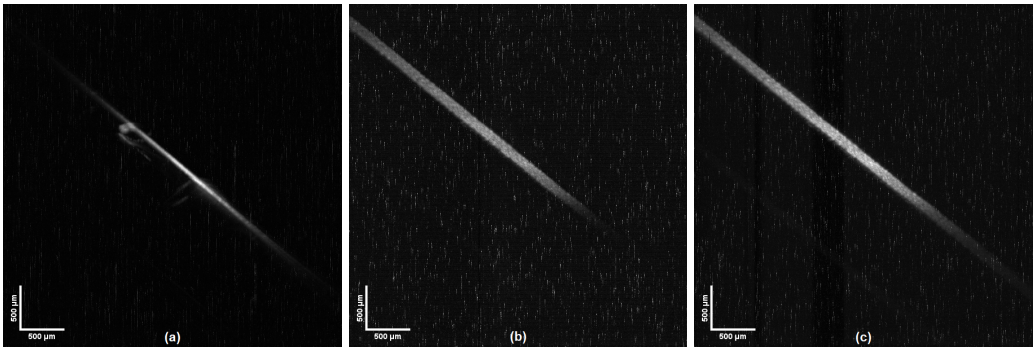

Figure 4.4: Photoacoustic images of a 45-degree prism with (a) Gaussian Beam, (b) Bessel Beam, and (c) Droplet Beam

Beam $\approx 2200\mu m$. A demanding reader would be able to spot two "problems" from those numbers. The first is that the different DOFs are far greater than the ones described earlier. Indeed this is true because for photoacoustic imaging to be carried we require a medium in which the ultrasound waves are going to propagate. This medium is deionized water, the refractive index of which is about ≈ 1.33 and much greater than air's which is ≈ 1. Therefore we expect to see a DOF far greater for all three cases. The second "problem" is that the Bessel Beam has a superior DOF than the Droplet Beam. This result was also expected as the latter is a result of the interference of two different Bessel Beams with two different DOFs each, so the final DOF will have some value between the two. Also, the background noise is far greater in the case of the Bessel Beam as clearly seen from the comparison of the two images above, which proves the point that through the cancellation of the side lobes, the obtained image quality would be improved. In these images again the power used was about double the one of the Gaussian beam but the results show a clear improvement in the image quality for the case of the Droplet beam so we expect to lower the power without dropping the contrast of the image.

Chapter 5

CONCLUSION

As we approach the completion of our research and experimental process regarding the limits of this Master's thesis, it would be beneficial to provide a recap of our results. By initially, developing a dedicated experimental setup to produce and study a Bessel Beam, we were able to characterize it. The beam was in complete agreement with both the theoretical expectations and the simulated results. By studying the effects of scattering for both a Bessel and a Gaussian Beam we were able to conclude that the Bessel Beam takes a heavier toll by the scattering effect which is expected as its intensity distribution is more complex than its Gaussian counterpart and scattering produces interference between the concentric peripheral rings leading to more significant disturbance of its intensity distribution and therefore steeper loss of the initial shape of the beam.

The extended Depth Of Field of a Bessel Beam proves to be a great asset for photoacoustic imaging as it provides constant resolution for greater depths. Despite this, the presence of a great portion of the total beam's energy in the peripheral rings forces us to use significantly more power for obtaining photoacoustic images with a Bessel beam than with a Gaussian one. The interferometric setup described thoroughly in Chapter 3 can provide a new cost-effective way of producing a so-called Droplet beam. This Droplet beam, due to the suppressed side lobes it comprises, can retain the much-extended Depth Of Field of a Bessel Beam, without carrying unexploited energy in the outer rings. Due to this, it can play a vital role in lowering the power of photoacoustic imaging. Early photoacoustic images have shown indeed this capability and the extent we can exploit this beam remains to be proven. Future research should be carried out regarding the aforementioned claims with the ultimate goal of finally acquiring images of not only ex vivo biological

samples but also in vivo.

BIBLIOGRAPHY

[1] Anat London, Inbal Benhar, and Michal Schwartz. “The retina as a window to the brain—from eye research to CNS disorders”. In: *Nature Reviews Neurology* 9.1 (2013), pp. 44–53.

[2] Giuseppe Di Domenico, Giancarlo Ruocco, Cristina Colosi, Eugenio DelRe, and Giuseppe Antonacci. “Cancellation of Bessel beam side lobes for high-contrast light sheet microscopy”. In: *Scientific reports* 8.1 (2018), pp. 1–7.

[3] Lihong V Wang and Hsin-i Wu. *Biomedical optics: principles and imaging*. John Wiley & Sons, 2012.

[4] Roarke Horstmeyer, Haowen Ruan, and Changhuei Yang. “Guidestar-assisted wavefront-shaping methods for focusing light into biological tissue”. In: *Nature photonics* 9.9 (2015), pp. 563–571.

[5] RH Freeman and James E Pearson. “Deformable mirrors for all seasons and reasons”. In: *Applied Optics* 21.4 (1982), pp. 580–588.

[6] Byoungyoul Park. “Development of a low voltage and large stroke MEMS-based lorentz force continuous deformable polymer mirror system”. In: (2018).

[7] Michael J Steinbock. *Implementation of branch-point-tolerant wavefront reconstructor for strong turbulence compensation*. Tech. rep. AIR FORCE INST OF TECH WRIGHT-PATTERSON AFB OH GRADUATE SCHOOL OF . . ., 2012.

[8] Dana Dudley, Walter M Duncan, and John Slaughter. “Emerging digital micromirror device (DMD) applications”. In: *MOEMS display and imaging systems*. Vol. 4985. SPIE. 2003, pp. 14–25.

[9] Uzi Efron. *Spatial light modulator technology: materials, devices, and applications*. Vol. 47. CRC press, 1994.

[10] Ashton S Hemphill, Jian Wei Tay, and Lihong V Wang. “Hybridized wavefront shaping for high-speed, high-efficiency focusing through dynamic diffusive media”. In: *Journal of Biomedical Optics* 21.12 (2016), pp. 121502–121502.

[11] HOLOEYE. *Holoeye pluto 2.1 spatial light modulator*. [Online; accessed April 20, 2023]. URL: https://holoeye.com/slm-pluto-phase-only/.

[12] Oto Brzobohatỳ, Tomáš Čižmár, and Pavel Zemánek. “High quality quasi-Bessel beam generated by round-tip axicon”. In: *Optics express* 16.17 (2008), pp. 12688–12700.

[13] Thorlabs. *Axicons, UV Fused Silica*. [Online; accessed April 28, 2023]. URL: https://www.thorlabs.com/newgrouppage9.cfm?objectgroup_id=4277.

[14] Joel Kubby, Sylvain Gigan, and Meng Cui. *Wavefront shaping for biomedical imaging*. Cambridge University Press, 2019.

[15] Thorlabs. *P500K - Ø1" Mounted Pinhole*. [Online; accessed April 28, 2023]. URL: https://www.thorlabs.com/thorproduct.cfm?partnumber=P500K.

[16] David Vilkomerson. “Acoustic imaging with thin annular apertures”. In: *Acoustical Holography: Volume 5* (1974), pp. 283–316.

[17] Thorlabs. *R1CA1000 Annular Aperture*. [Online; accessed May 23, 2023]. URL: https://www.thorlabs.com/newgrouppage9.cfm?objectgroup_id=8531.

[18] Joseph Thomas Verdeyen. “Laser electronics”. In: (1989).

[19] Wikipedia contributors. *Gaussian beam — Wikipedia, The Free Encyclopedia*. https://en.wikipedia.org/wiki/Gaussian_beam. [Online; accessed 07-May-2023]. 2023.

[20] Dimitris Papazoglou. *FOundation of Modern Optics*. 2021.

[21] Université du Maine. *Hermite-Gaussian Modes*. [Online; accessed May 7, 2023]. 2009. URL: http://www.optique-ingenieur.org/en/courses/OPI_ang_M01_C03/co/Contenu_13.html.

[22] Michael V Berry and Nandor L Balazs. "Nonspreading wave packets". In: *American Journal of Physics* 47.3 (1979), pp. 264–267.

[23] GA Siviloglou, J Broky, Aristide Dogariu, and DN Christodoulides. "Observation of accelerating Airy beams". In: *Physical Review Letters* 99.21 (2007), p. 213901.

[24] JJJM Durnin, JJ Miceli Jr, and Joseph H Eberly. "Diffraction-free beams". In: *Physical review letters* 58.15 (1987), p. 1499.

[25] JJJA Durnin. "Exact solutions for nondiffracting beams. I. The scalar theory". In: *JOSA A* 4.4 (1987), pp. 651–654.

[26] MR Lapointe. "Review of non-diffracting Bessel beam experiments". In: *Optics & Laser Technology* 24.6 (1992), pp. 315–321.

[27] AJ Cox and Dean C Dibble. "Nondiffracting beam from a spatially filtered Fabry–Perot resonator". In: *JOSA A* 9.2 (1992), pp. 282–286.

[28] Xiaoming Yu, Meng Zhang, and Shuting Lei. "Multiphoton polymerization using femtosecond Bessel beam for layerless three-dimensional printing". In: *Journal of Micro and Nano-Manufacturing* 6.1 (2018).

[29] Guy Indebetouw. "Nondiffracting optical fields: some remarks on their analysis and synthesis". In: *JOSA A* 6.1 (1989), pp. 150–152.

[30] Christian Vetter, Ralf Steinkopf, Klaus Bergner, Marco Ornigotti, Stefan Nolte, Herbert Gross, and Alexander Szameit. "Realization of Free-Space Long-Distance Self-Healing Bessel Beams". In: *Laser & Photonics Reviews* 13.10 (2019), p. 1900103.

[31] Jakub Czuchnowski and Robert Prevedel. “Photoacoustics: seeing with sound Understand article”. In: ().

[32] Junjie Yao, Konstantin I Maslov, Yunfei Shi, Larry A Taber, and Lihong V Wang. “In vivo photoacoustic imaging of transverse blood flow by using Doppler broadening of bandwidth”. In: *Optics letters* 35.9 (2010), pp. 1419–1421.

[33] Scott A Prahl, Martin JC van Gemert, and Ashley J Welch. “Determining the optical properties of turbid media by using the adding–doubling method”. In: *Applied optics* 32.4 (1993), pp. 559–568.